Phenomenology of the flavor symmetric scoto-seesaw model with dark matter and TM_1 mixing

Joy Ganguly,[1,*] Janusz Gluza,[2,†] Biswajit Karmakar,[2,‡] and Satyabrata Mahapatra[3,§]

[1]*Department of BSH, University of Engineering and Management, Kolkata, India*
[2]*Institute of Physics, University of Silesia, Katowice, Poland*
[3]*Department of Physics and Institute of Basic Science, Sungkyunkwan University, Suwon 16419, Korea*

(Received 20 February 2024; accepted 26 June 2024; published 9 August 2024)

We propose a hybrid scoto-seesaw model based on the $A_4 \times Z_4 \times Z_3 \times Z_2$ non-Abelian discrete flavor symmetry. Light neutrino masses come from the tree-level type-I seesaw mechanism, and from the one-loop scotogenic contribution accommodating viable dark matter candidates responsible for the observed relic abundance of dark matter (DM). These contributions restore the atmospheric and solar neutrino mass scales, respectively. With only one right-handed neutrino, the model features specific predictions with the normal ordering of light neutrino masses, the lightest neutrino being massless, and only one relevant *CP* Majorana phase. Further, an experimentally favorable TM_1 mixing scheme is realized with concrete correlations and constraints on the mixing angles and associated *CP* phases. The model predicts the atmospheric mixing angle to be in the upper octant with specific ranges $0.531(0.580) \leq \sin^2\theta_{23} \leq 0.544(0.595)$, and the Dirac *CP* phase is restricted within the range $\pm(1.44\text{–}1.12)$ rad. The Majorana phase is also tightly constrained, with the ranges 0.82–0.95 and 1.58–1.67 rad, which are otherwise unconstrained from neutrino oscillations. Strict predictions on the Majorana phases also yield an accurate prediction for the effective mass parameter for neutrinoless double beta within the range of 1.61–3.85 meV. The model offers a rich phenomenology regarding DM relic density and direct-search constraints, and the fermionic DM scenario has been discussed in detail, estimating its possible connection with the neutrino sector. As an example of the model studies at colliders, the SM Higgs in the diphoton decay channel is examined. The model predicts strictly vanishing $\tau \to e\gamma$, $\tau \to 3e$ decays and testable signals by MEG-II and SINDRUM/Mu3e experiments for the $\mu \to e\gamma$ and $\mu \to 3e$ decays, respectively.

DOI: 10.1103/PhysRevD.110.035012

I. INTRODUCTION

In the last few decades, several experiments around the globe have confirmed the phenomenon of neutrino oscillation with incredible precision [1–8]. The immediate consequence of neutrino oscillation is that at least two light neutrinos have nonzero mass. Furthermore, if we combine this with a bound on the absolute neutrino masses coming from the end-point spectrum of the tritium beta decay [9], as well as the bounds from cosmological surveys [10] and the neutrinoless double beta decay [11], we conclude that the neutrino masses are in the sub-eV scale. Despite these spectacular accomplishments, the origin of tiny neutrino masses (compared to other Standard Model fermions) remains an open question in particle physics. Over the years, various ideas have been proposed, and the most common schemes are seesaw mechanisms [12–19] and the radiative generation of neutrino masses [20]. Nonzero neutrino masses can also be realized within the framework of hybrid mass mechanisms where both seesaw and radiative mass mechanisms contribute.

In addition to the tiny neutrino masses, we are yet to understand the observed pattern of the lepton mixing comprehensively. In fact, two of the three mixing angles—namely, solar (θ_{12}) and atmospheric (θ_{23})—are found to be large, while the reactor (θ_{13}) mixing angle is relatively small. Such a finding clearly shows the distinctive feature associated with the lepton sector in contrast to the quark sector. The study of the underlying principle behind this typical mixing is particularly interesting with the precise measurement of the reactor mixing angle θ_{13} [7,8,21,22]. Neutrino oscillation data also constrains the two mass-squared differences (solar and atmospheric) defined as $\Delta m^2_{21} = m^2_2 - m^2_1$ and $|\Delta m^2_{31}| = |m^2_3 - m^2_1|$, where m_1, m_2,

*Contact author: joyganguly.hep2022@gmail.com
†Contact author: janusz.gluza@us.edu.pl
‡Contact author: biswajit.karmakar@us.edu.pl
§Contact author: satyabrata@g.skku.edu

m_3 are the masses of the three light neutrinos. The present global analysis from several experimental data can be summarized as [23]

$$\begin{aligned}
&\Delta m^2_{21} = (6.82 - 8.03) \times 10^{-5}\ \text{eV}^2,\\
&|\Delta m^2_{31}| = (2.427 - 2.590) \times 10^{-3}\ \text{eV}^2,\\
&\sin^2\theta_{12} = 0.270 - 0.341, \qquad \sin^2\theta_{23} = 0.408 - 0.603,\\
&\sin^2\theta_{13} = 0.02052 - 0.02398
\end{aligned} \tag{1}$$

for normal ordering (NO) of light neutrino masses, and similar constraints for inverted ordering (IO) [23]. In this regard, many conjectures have been put forward. A particular pattern yielding $\sin^2\theta_{23} = 1/2$, $\sin^2\theta_{12} = 1/3$, and $\theta_{13} = 0$, known as tri-bimaximal mixing (TBM) [24], received a lot of attention due to the proximity of θ_{23} and θ_{12} with experimental values. Such a mixing pattern can also be elegantly generated using flavor symmetries. Particularly, the use of non-Abelian discrete symmetries like S_3, A_4, S_4, A_5 is very well known [25,26] in this context. For a detailed discussion on such frameworks, see [27–32] and references therein. Unsurprisingly, a deformation from TBM mixing becomes inevitable after precisely measuring θ_{13}. Nevertheless, the TBM mixing scheme can still be considered as a leading-order approximation, requiring adjustments such as accounting for nonzero θ_{13} and the Dirac CP phase δ. Possible simple deviations from the TBM mixing are called trimaximal (TM_1 and TM_2) mixings, where the first and second columns of the TBM mixing, respectively, remain identical [33–41]. Such deviations can be elegantly achieved by considering larger residual symmetry (compared to the TBM scenario) or introducing an additional constituent that breaks the TBM structure [40–49]. Although the 3σ allowed ranges for all three mixing angles can be explained by both TM_1 and TM_2 mixings, the allowed value of the solar mixing angle θ_{12} (within these trimaximal scenarios) slightly prefers the TM_1 over the TM_2 mixing scheme. For a detailed discussion on the relative comparison of both mixings, see [32].

Apart from the neutrino masses and mixing, unraveling the nature of dark matter (DM) remains a pressing challenge in contemporary particle physics. While compelling astrophysical evidence, including observations like galaxy rotation curves, gravitational lensing, and the cosmic large-scale structure, substantiates the existence of DM [50], the quest for a laboratory-based confirmation persists. Satellite missions such as WMAP [51] and *Planck* [52] have precisely determined that DM constitutes roughly 26.8% of the total energy content of the Universe. Expressing the prevailing dark matter abundance through the density parameter Ω_{DM} and the normalized Hubble parameter h (the Hubble parameter divided by 100 $\text{km}\,\text{s}^{-1}\,\text{Mpc}^{-1}$) yields $\Omega_{\text{DM}}h^2 = 0.120 \pm 0.001$ at a 68% confidence level. Still, the intricacies of its properties beyond gravitational interactions remain elusive. Among all proposed particle dark matter, the most sought-after paradigm is the weakly interacting massive particle (WIMP) paradigm, which suggests a dark matter particle with a mass and interaction strength akin to the electroweak scale. Unfortunately, the Standard Model of particle physics fails to comprehensively explain either neutrino masses and mixings, or dark matter. Standing at this juncture, certainly, it is a tempting challenge to find a common origin of these two seemingly uncorrelated sectors, if any. Hence, we aim to go beyond the SM of particle physics to explore scenarios that can accommodate a candidate of DM and explain nonzero neutrino masses and mixings.

Neutrino oscillation data presented earlier [see Eq. (1)] does not determine the absolute scale or ordering of neutrino masses. The experiments have measured the two mass-squared differences (solar and atmospheric) associated with neutrino oscillations, and the ratio of the solar to atmospheric mass-squared difference (r) is found to be [23]

$$r = \Delta m^2_{21}/|\Delta m^2_{31}| \sim 0.03. \tag{2}$$

This may be an indication of the involvement of two different mass scales that might originate from entirely separate mechanisms.[1] Following this ethos, the authors in [61] showed a scotogenic extension of the type-I seesaw scenario that can minimally explain the hierarchy of solar and atmospheric neutrino mass scales. In this setup, the Standard Model particle content is extended by including one heavy isosinglet neutral lepton N_R (for the type-I sector) along with a dark fermion f and an inert scalar doublet η (for the scotogenic sector), both being odd under a dark Z_2 symmetry. Here, the type-I contribution gives rise to the larger atmospheric scale. In contrast, the one-loop scotogenic contribution turns out to be the origin of the smaller solar mass scale mediated by a dark fermion, also providing a potential dark matter candidate [62,63]. Unfortunately, such constructions turn out to be inadequate in explaining the observed neutrino oscillation data associated with the mixing and the Dirac CP phase mentioned above. This problem can be addressed by augmenting well-motivated non-Abelian discrete flavor symmetries. Earlier, in [64,65], the authors proposed a flavor symmetric realization of the scoto-seesaw framework with two right-handed neutrinos having Z_8 and A_4 discrete symmetries. The use of A_4 discrete flavor symmetry has the additional advantage of obtaining analytic expressions for neutrino

[1]Within the framework of the type-I seesaw mechanism, the hierarchy of the atmospheric and solar neutrino mass scales can also be explained through the mechanisms of sequential dominance [53–58] and constrained sequential dominance [59,60], where one of the right-handed neutrinos is considered to dominantly contribute the light neutrino masses.

masses and mixing angles, as well as yielding interesting correlations among the oscillation parameters with distinctive predictions. For instance, in [65], the authors realized a TM_2 mixing scheme within a flavor symmetric scoto-seesaw (FSS) framework with A_4 symmetry, which can arise in various ways such as starting from a continuous [66–71] or superstring theory in compactified extra dimensions [26,43,72–81]. Furthermore, in another A_4-based scoto-seesaw framework [82], the authors showed that the hierarchy of atmospheric and solar neutrino mass splitting can be obtained as a prediction of the "discrete dark matter" mechanism [83]. In this construction, both the scotogenic contribution and the stabilizing symmetry for DM (obtained as a residual symmetry of A_4 breaking) appear naturally; however, additional copies of right-handed neutrinos and scalar doublets are essential.

In the present work, we show that the scoto-seesaw mechanism can be embedded within a $A_4 \times Z_4 \times Z_3 \times Z_2$ flavor symmetric framework with the involvement of *only one right-handed neutrino*, and the *experimentally favored* TM_1 *mixing scheme* can be realized. We will call the present model FSS_1 from now on, as it explains the TM_1 mixing scheme. The scotogenic contribution contains neutral particles in both the fermionic and scalar sectors. Within this flavor symmetric framework, we perform a phenomenological study of the fermionic dark matter and determine its correlation with the observed neutrino mixing. The obtained magnitude and flavor structure of the scotogenic contribution dictates the observed neutrino mixing pattern and facilitates us in obtaining the correct dark matter relic density. Such a direct correlation with the dark matter sector was missing in [65]; a detailed analysis on fermionic dark matter in this work also completes the associated phenomenology. The presence of flavor symmetry makes an interesting prediction for the neutrino mass hierarchy, determines the octant of the atmospheric mixing angle θ_{23}, and tightly constrains the TM_1 prediction for the Dirac CP phase δ_{CP}. Here, the type-I contribution produces a neutrino mass matrix of rank 1, yielding only one massive light neutrino. Subsequently, the scotogenic contribution generates another neutrino mass eigenstate, and together, we obtain two massive neutrinos, which follow the normal ordering of the light neutrino mass spectrum. In [61], the authors showed that the type-I and scotogenic contributions could be the origin of the atmospheric and solar mass scales. Here, we show that such a hierarchy can also be procured within a flavor symmetric construction, explaining observed neutrino oscillation data. Furthermore, in the present model, we can obtain the constraint on the Majorana phase and predict the effective mass parameter appearing in the neutrinoless double beta decay and the sum of the absolute neutrino masses.

One of the essential aspects of any theoretical model is its experimental viability. For the version of the FSS model discussed here, we perform a comprehensive phenomenological analysis involving the $h \to \gamma\gamma$ decay, where h is the SM Higgs boson. The signal strength of the Higgs in the diphoton decay channel, $R_{\gamma\gamma}$, is measured at the LHC, the value of which is around 1 [84]. The additional contribution to the decay of $h \to \gamma\gamma$ in the FSS_1 model is the charged scalar of the η field. Our analysis shows that $R_{\gamma\gamma}$ can be fitted in our model, which can constrain the mass of the charged component of the η field. Owing to the flavor structure of this scoto-seesaw framework, we find that only the scotogenic part contributes to the lepton-flavor-violating decays such as $\mu \to e\gamma$, $\mu \to 3e$, whereas only the seesaw part contributes in the decays such as $\tau \to \mu\gamma$, $\tau \to 3\mu$. However, the scotogenic and seesaw parts do not contribute to the $\tau \to e\gamma$ or $\tau \to 3e$ decays, a distinctive feature of the present construction. All these phenomenological analyses for the FSS_1 framework serve as crucial tests of the model's predictions and provide valuable insights into its compatibility with experimental data.

The rest of the paper is organized as follows: In Sec. II, we briefly introduce the minimal scoto-seesaw framework. In Sec. III, we present the complete A_4 flavor symmetric scoto-seesaw scenario, and in Sec. IV, we analyze corresponding neutrino masses and mixing. We mention the low-energy scalar potential in Sec. V. In Sec. VI, we discuss the detailed phenomenology of fermionic dark matter, and we further explore phenomenological implications for the Higgs to the diphoton decay and lepton flavor violation in Secs. VII and VIII, respectively. Then, in Sec. IX, we summarize the phenomenological analysis. Finally, in Sec. X, we present the conclusion and outlook of the FSS_1 framework.

II. MINIMAL SCOTO-SEESAW MODEL

In this section, we present the minimal scoto-seesaw model which is introduced in [61]. The minimal scoto-seesaw model consists of one[2] right-handed neutrino N_R, one singlet dark fermion f, and one extra scalar doublet η_R. In addition to these particles, one Z_2 symmetry is introduced to stabilize the dark matter. In this model,[3] the usual type-I seesaw mechanism with one right-handed neutrino N_R is combined with the scotogenic model with fermion f. The type-I seesaw generates the atmospheric mass scale at the tree level, while the solar mass scale is generated at the loop level in the scotogenic mechanism. As a result, the hierarchy between the solar mass scale and the atmospheric mass scale is maintained. The relevant Lagrangian in the model can be written as

[2]The number of right-handed neutrinos added [18] to the SM is not fixed, as they do not carry any anomaly [85].

[3]For various extensions of the minimal scoto-seesaw scenario, see Refs. [62–65,86–89].

$$\mathcal{L} = -Y_N^k \bar{L}^k i\sigma_2 H^* N_R + \frac{1}{2} M_N \bar{N}_R^c N_R + Y_f^k \bar{L}^k i\sigma_2 \eta^* f + \frac{1}{2} M_f \bar{f}^c f + \text{H.c.}, \tag{3}$$

where L^k are the lepton doublets. The scalars H and η are the $SU(2)$ doublets defined in Eq. (35). Y_N and Y_f are complex 3×1 Yukawa coupling matrices, and $M_{N,f}$ are the mass terms for N_R and f. The total neutrino mass reads [61]

$$M_\nu^{ij} = -\frac{v^2}{M_N} Y_N^i Y_N^j + \mathcal{F}(M_{\eta_R}, M_{\eta_I}, M_f) M_f Y_f^i Y_f^j. \tag{4}$$

Here, the first term is due to the tree-level seesaw mechanism, while the second term originates from the one-loop scotogenic contribution with

$$\mathcal{F}(M_{\eta_R}, M_{\eta_I}, M_f) = \frac{1}{32\pi^2}\left[\frac{M_{\eta_R}^2 \log(M_f^2/M_{\eta_R}^2)}{M_f^2 - M_{\eta_R}^2} - \frac{M_{\eta_I}^2 \log(M_f^2/M_{\eta_I}^2)}{M_f^2 - M_{\eta_I}^2}\right], \tag{5}$$

where M_{η_R} and M_{η_I} are the masses of the neutral component of η. Although the ratio of the above two contributions in Eq. (4) can explain the hierarchy of the solar and atmospheric mass scales, it fails to explain the observed neutrino mixing pattern. In this regard, the use of non-Abelian discrete flavor symmetries is well motivated [28–32]. In the following sections, we discuss the phenomenological consequences of flavor-symmetric construction of the scoto-seesaw framework with only one right-handed neutrino to explain the correct neutrino masses and mixing. We also provide a detailed analysis of the fermionic dark matter relic abundance and direct detection search constraint to determine the parameter space consistent with neutrino oscillation data and predictions for Higgs-to-diphoton signal strength and lepton-flavor-violating decays.

III. SCOTO-SEESAW WITH FLAVOR SYMMETRY: THE FSS_1 MODEL

The model we are proposing is the flavor-symmetric version of the scoto-seesaw model described in the previous section with the usual scotogenic fermion f and inert doublet η in addition to one right-handed neutrino N_R. To obtain the flavor structure, $A_4 \times Z_4 \times Z_3 \times Z_2$ flavor discrete symmetry and flavons ϕ_s, ϕ_a, ϕ_T, and ξ are introduced. To avoid unwanted terms in the Lagrangian and get the correct flavor Yukawa structure, additional Z_N symmetries are introduced. The inclusion of flavon fields and auxiliary symmetries are generic features of such flavor-symmetric constructions [25,26,72,90]. A remnant Z_2 symmetry of the Z_N symmetries acts as a dark symmetry that ensures the stability of dark matter under which only f and η are odd. Similar types of flavored scoto-seesaw models were studied before in [64,65] with Z_8 and $A_4 \times Z_4 \times Z_3 \times Z_2$ discrete symmetries, respectively. No simple analytic correlation can be obtained due to the use of the Z_8 symmetry [64], whereas the TM_2 mixing was reproduced in [65] with the $A_4 \times Z_4 \times Z_3 \times Z_2$ symmetry. In both cases, two right-handed neutrinos are introduced in the seesaw contribution to get the flavor structure and mixing. In the present work, we construct the framework with only one right-handed neutrino and realize the experimentally preferred TM_1 mixing scheme compared to the TM_2 mixing scheme (derived in [65]). The particle content of our model and charge assignment under different symmetries are shown in Table I. The role of each discrete auxiliary symmetry will be described in detail as we proceed further.

TABLE I. Field content and transformations under the symmetries of the FSS_1 model. Product rules of the A_4 singlets and triplets are given in the Appendix. The flavon fields mentioned in the second block are essential to implement the A_4 symmetry, and $\omega(= e^{2i\pi/3})$ is the cube root of unity.

Fields	e_R, μ_R, τ_R	L_α	H	N_R	f	η	ϕ_s	ϕ_a	ϕ_T	ξ
A_4	$1, 1'', 1'$	3	1	1	1	1	3	3	3	$1''$
Z_4	-1	i	1	1	1	1	i	i	$-i$	1
Z_3	1	ω	ω	1	1	1	ω^2	ω	1	1
Z_2	-1	1	1	1	-1	-1	1	-1	-1	-1

With the field content and charge assignment in Table I, the charged lepton Lagrangian can be written up to leading order as

$$\mathcal{L}_l = \frac{y_e}{\Lambda}(\bar{L}\phi_T) H e_R + \frac{y_\mu}{\Lambda}(\bar{L}\phi_T) H \mu_R + \frac{y_\tau}{\Lambda}(\bar{L}\phi_T) H \tau_R + \text{H.c.}, \tag{6}$$

where Λ is the cutoff scale of our model. y_e, y_μ, and y_τ are the coupling constants. Now, when the flavon ϕ_T gets a vacuum expectation value (VEV) in the direction $\langle \phi_T \rangle = (v_T, 0, 0)^T$ and subsequently, the Higgs field also gets a VEV as $\langle H \rangle = v$, where v is the SM VEV, we find the charged lepton mass matrix to be in the diagonal form as

$$M_l = \frac{v_T}{\Lambda} v \begin{pmatrix} y_e & 0 & 0 \\ 0 & y_\mu & 0 \\ 0 & 0 & y_\tau \end{pmatrix}. \tag{7}$$

Now, the Lagrangian in the neutrino sector, which generates neutrino masses, constitutes two parts: a type-I seesaw contribution with one right-handed neutrino N_R, and another one-loop scotogenic part with the presence of the dark fermion f and scalar η. Following the symmetries and particle content mentioned in Table I, the Lagrangian for the neutrino sector can be written as

$$\mathcal{L} = \frac{y_N}{\Lambda}(\bar{L}\phi_s)\tilde{H}N_R + \frac{1}{2}M_N\bar{N}_R^c N_R + \frac{y_s}{\Lambda^2}(\bar{L}\phi_a)\xi i\sigma_2\eta^* f + \frac{1}{2}M_f\bar{f}^c f + \text{H.c.}, \tag{8}$$

where y_N and y_s are the coupling constants and M_N is the Majorana mass of the right-handed neutrino N_R, while M_f is the mass of the fermion f. In the above Lagrangian, we have considered VEVs of the flavons ϕ_s, ϕ_a, and ξ in the directions $\langle\phi_s\rangle = (0, -v_s, v_s)$, $\langle\phi_a\rangle = (2v_a, v_a, 0)$, and $\langle\xi\rangle = v_\xi$, respectively. A similar vacuum alignment can be found in the literature for neutrino model building [60,91], which can be realized inherently by analyzing the complete scalar potential [28,48,59,92–94]. The light neutrino mass matrix involving both type-I seesaw and scotogenic contributions can be written as

$$(M_\nu)_{ij} = -\frac{v^2}{M_N}Y_N^i Y_N^j + \mathcal{F}(M_{\eta_R}, M_{\eta_I}, M_f)M_f Y_f^i Y_f^j, \tag{9}$$

where the Yukawa couplings take the following form:

$$Y_N = (Y_N^e, Y_N^\mu, Y_N^\tau)^T = \left(0, y_N\frac{v_s}{\Lambda}, -y_N\frac{v_s}{\Lambda}\right)^T, \tag{10}$$

$$Y_F = (Y_F^e, Y_F^\mu, Y_F^\tau)^T = \left(y_s\frac{v_\xi}{\Lambda}\frac{v_a}{\Lambda}, y_s\frac{v_\xi}{\Lambda}\frac{2v_a}{\Lambda}, 0\right)^T \equiv (\kappa, 2\kappa, 0)^T. \tag{11}$$

Within this setup, the total effective light neutrino mass matrix of Eq. (9) is the following:

$$M_\nu = \begin{pmatrix} b & 2b & 0 \\ 2b & -a+4b & a \\ 0 & a & -a \end{pmatrix}, \tag{12}$$

with

$$a = y_N^2\frac{v^2}{M_N}\frac{v_s^2}{\Lambda^2}, \tag{13}$$

$$b = y_s^2\frac{v_\xi^2}{\Lambda^2}\frac{v_a^2}{\Lambda^2}\mathcal{F}(m_{\eta_R}, m_{\eta_I}, M_f)M_f \equiv \kappa^2\mathcal{F}(M_{\eta_R}, M_{\eta_I}, M_f)M_f, \tag{14}$$

where $\mathcal{F}$ is the loop function defined in Eq. (5). Clearly, from Eqs. (10)–(14), it is evident that the parameters a and b originate from type-I seesaw and scotogenic contributions, respectively. In the next section, we show how these parameters' relative magnitudes help us explain the hierarchy of the atmospheric and solar oscillation mass scales.

Though the neutrino mass matrix given in Eq. (12) is obtained through a combination of type-I seesaw and scotogenic mechanisms, there can be additional operators like $LHLH/\Lambda$, contributing to the light neutrino masses. In our model, this higher-dimensional term is not invariant explicitly under the Z_4 symmetry given in Table I. Also, terms like $LHLH(\phi_a, \phi_s, \phi_T, \xi)/\Lambda^2$ are disallowed due to the considered discrete Z_N symmetries. For the same Z_N symmetries, the scotogenic contribution $(\bar{L}i\sigma_2\eta^* f)$ is only allowed at $1/\Lambda^2$ with the involvement of flavons ϕ_a and ξ, which are both odd under the Z_2 symmetry along with f and η. Here, in principle, there could be another contributing term via $\bar{L}i\sigma_2\eta^* f\phi_a\xi^\dagger/\Lambda^2$. This term, however, can be absorbed in the previous contribution through a redefinition of the Yukawa coupling. Owing to the A_4 symmetry, in the charged lepton sector, the leading-order contribution appears only at dimension 5. However, for example, there could be a next-to-leading correction at $\mathcal{O}(1/\Lambda^2)$ via $(\bar{L}\phi_s^\dagger\phi_a)H\alpha_R/\Lambda^2$, where α_R is the corresponding right-handed charged lepton. Interestingly, such a contribution is disallowed due to the Z_4 symmetry given in Table I. As the right-handed Majorana neutrino present in our model is also a singlet under A_4 symmetry, any higher-order correction can be absorbed in the leading-order contribution to M_N. For the same reason, we can also absorb any higher-order contribution to M_f, as it does not affect the flavor structure of our model. Finally, the Dirac Yukawa coupling is allowed at dimension 5, as given in Eq. (11). The next-to-leading-order contributions at $\mathcal{O}(1/\Lambda^2)$, such as $(\bar{L}\phi_a^\dagger\phi_T)\tilde{H}N_R$ and $(\bar{L}\phi_s^\dagger\phi_T)\tilde{H}N_R$, are not allowed due to the Z_4 symmetry.

IV. NEUTRINO MASSES AND MIXINGS IN THE FSS$_1$ MODEL

The model we presented in the last section has two parts. One is coming from a type-I seesaw with one right-handed neutrino N_R. Another part is the scotogenic contribution with the dark fermion f. The full light neutrino mass matrix is given in Eq. (12), and both contributions are essential in explaining observed neutrino masses and mixing. To diagonalize the mass matrix in Eq. (12), we first write the mass matrix in the TBM basis as

$$M'_\nu = U_{\text{TB}}^T M_\nu U_{\text{TB}} = \begin{pmatrix} 0 & 0 & 0 \\ 0 & 3b & -\sqrt{6}b \\ 0 & -\sqrt{6}b & 2(b-a) \end{pmatrix}, \tag{15}$$

where

$$U_{\text{TB}} = \begin{pmatrix} \sqrt{\frac{2}{3}} & \sqrt{\frac{1}{3}} & 0 \\ -\sqrt{\frac{1}{6}} & \sqrt{\frac{1}{3}} & -\sqrt{\frac{1}{2}} \\ -\sqrt{\frac{1}{6}} & \sqrt{\frac{1}{3}} & \sqrt{\frac{1}{2}} \end{pmatrix}. \tag{16}$$

As is evident from Eq. (15), a further rotation by U_{23} (another unitary matrix) in the 23 plane will diagonalize the light neutrino mass matrix via $M_\nu^{\rm diag} = U_{23}^T M'_\nu U_{23}$. The unitary rotation matrix U_{23} can be parametrized as

$$U_{23} = \begin{pmatrix} 1 & 0 & 0 \\ 0 & \cos\theta & \sin\theta e^{-i\psi} \\ 0 & -\sin\theta e^{i\psi} & \cos\theta \end{pmatrix}, \tag{17}$$

where θ and ψ are the rotation angle and the associated phase factor, respectively. So, the diagonalization of M_ν can be achieved through

$$(U_{\rm TB}U_{23})^T M_\nu (U_{\rm TB}U_{23}) = {\rm diag}(m_1 e^{i\gamma_1}, m_2 e^{i\gamma_2}, m_3 e^{i\gamma_3}), \tag{18}$$

where $m_{1,2,3}$ are the real and positive mass eigenvalues, and $\gamma_{1,2,3}$ are the phases that are extracted from the corresponding complex eigenvalues. In our framework, we have only one right-handed neutrino, which, via type-I seesaw [the first term in Eq. (9)], yields a rank-1 mass matrix which makes one light neutrino massive. Together with the scotogenic contribution, we obtain a rank-2 mass matrix given in Eq. (12), generating two massive neutrinos. Hence, within this flavor-symmetric construction, one mass eigenvalue (the lightest) will be zero. So, we have $m_1 = 0$, which implies $\gamma_1 = 0$. Now, we can get the form of the neutrino mixing matrix U_ν such that $U_\nu^T M_\nu U_\nu = {\rm diag}(0, m_2, m_3)$. Thus, U_ν becomes $U_\nu = U_{\rm TB}U_{23}U_m$, where $U_m = {\rm diag}(1, 1, e^{i\alpha_{32}/2})$ is the Majorana phase matrix with $\alpha_{32} = \gamma_3 - \gamma_2$. Therefore, we have only one nonzero phase in the Majorana phase matrix U_m, as the lightest neutrino is massless. The explicit form of U_ν follows

$$U_\nu = \begin{pmatrix} \sqrt{\frac{2}{3}} & \frac{\cos\theta}{\sqrt{3}} & \frac{e^{-i\psi}\sin\theta}{\sqrt{3}} \\ -\frac{1}{\sqrt{6}} & \frac{\cos\theta}{\sqrt{3}} + \frac{e^{i\psi}\sin\theta}{\sqrt{2}} & -\frac{\cos\theta}{\sqrt{2}} + \frac{e^{-i\psi}\sin\theta}{\sqrt{3}} \\ -\frac{1}{\sqrt{6}} & \frac{\cos\theta}{\sqrt{3}} - \frac{e^{i\psi}\sin\theta}{\sqrt{2}} & \frac{\cos\theta}{\sqrt{2}} + \frac{e^{-i\psi}\sin\theta}{\sqrt{3}} \end{pmatrix} U_m. \tag{19}$$

This form of U_ν is well known in the literature as a deviation from $U_{\rm TBM}$ and is called the $\rm TM_1$ mixing pattern, where the first column of the lepton mixing matrix is trimaximal. The VEV alignment of the flavons $\phi_{a,s}$ mentioned earlier plays a crucial role in obtaining such a mixing pattern. The lepton mixing matrix U_ν can now be compared with $U_{\rm PMNS}$, which in its standard parametrization is given by [95]

$$U_{\rm PMNS} = \begin{pmatrix} c_{12}c_{13} & s_{12}c_{13} & s_{13}e^{-i\delta_{CP}} \\ -s_{12}c_{23} - c_{12}s_{23}s_{13}e^{i\delta_{CP}} & c_{12}c_{23} - s_{12}s_{23}s_{13}e^{i\delta_{CP}} & s_{23}c_{13} \\ s_{12}s_{23} - c_{12}c_{23}s_{13}e^{i\delta_{CP}} & -c_{12}s_{23} - s_{12}c_{23}s_{13}e^{i\delta_{CP}} & c_{23}c_{13} \end{pmatrix} U_m, \tag{20}$$

where $c_{ij} = \cos\theta_{ij}$, $s_{ij} = \sin\theta_{ij}$, δ_{CP} is the Dirac CP-violating phase, and U_m is the Majorana phase matrix. We can see that the total light neutrino mass matrix of Eq. (12) contains two parameters a and b associated with the type-I seesaw and scotogenic contributions, which can be complex in general. We can write these parameters as $a = |a|e^{i\phi_a}$ and $b = |b|e^{i\phi_b}$, where ϕ_a and ϕ_b are the associated phases. For calculational purposes, we define the parameter $\alpha = |a|/|b|$ and the difference of phases by $\phi_{ab} = \phi_a - \phi_b$. As M'_ν is diagonalized by U_{23}, the rotation angle θ and the phase ψ appearing in Eq. (17) can be expressed in terms of the model parameters as

$$\tan\psi = \frac{2\alpha\sin\phi_{ab}}{5 - 2\alpha\cos\phi_{ab}}, \qquad \tan 2\theta = \frac{2\sqrt{6}}{\cos\psi + 2\alpha\cos(\psi + \phi_{ab})}. \tag{21}$$

As the charged lepton mass matrix is diagonal, to obtain the correlation among the mixing angles and phases, we can compare $U_\nu = U_{\rm TB}U_{23}U_m$ of Eq. (19) with $U_{\rm PMNS}$ given in Eq. (20). These correlations can be written as [37–39]

$$\sin\theta_{13}e^{-i\delta_{CP}} = \frac{e^{-i\psi}\sin\theta}{\sqrt{3}}, \qquad \sin^2\theta_{12} = 1 - \frac{2}{3 - \sin^2\theta}, \qquad \sin^2\theta_{23} = \frac{1}{2}\left(1 - \frac{\sqrt{6}\sin 2\theta\cos\psi}{3 - \sin^2\theta}\right). \tag{22}$$

The above relations among the three mixing angles imply a mutual correlation. These correlations are the unique feature of the considered $A_4 \times Z_4 \times Z_3 \times Z_2$ flavor symmetry, giving rise to the $\rm TM_1$ mixing scheme. More specifically, relations in Eq. (22) are general for the $\rm TM_1$ mixing scheme [37–39], where the mixing angles θ_{13} and θ_{12} are being correlated to each other. The correlation plot among these mixing angles can be found in Ref. [38], where $\sin^2\theta_{12}$ is restricted to some narrow range corresponding to the 3σ regions of $\sin^2\theta_{13}$. Relations in Eq. (21) are unique for the considered $\rm FSS_1$ model. From Eqs. (21) and (22), it is clear that the angle θ and the associated phase

ψ in U_{23} can be linked with the parameters involved in M_ν. Relations in Eq. (22) imply that $\delta_{CP} = \psi$ when $\sin\theta > 0$, and $\delta_{CP} = \psi \pm \pi$ for $\sin\theta < 0$, which can be written in a compact form as $\tan\delta_{CP} = \tan\psi$. Now, from Eq. (12), the complex mass eigenvalues are calculated to be

$$m_1^c = 0, \tag{23}$$

$$m_2^c = \frac{1}{2}\left(-2a + 5b - \sqrt{4a^2 + 4ab + 25b^2}\right), \tag{24}$$

$$m_3^c = \frac{1}{2}\left(-2a + 5b + \sqrt{4a^2 + 4ab + 25b^2}\right). \tag{25}$$

The real and positive mass eigenvalues are calculated as

$$m_1 = 0, \tag{26}$$

$$m_2 = \frac{|b|}{2}[(5 - 2\alpha\cos\phi_{ab} - P)^2 + (Q + 2\alpha\sin\phi_{ab})^2]^{1/2}, \tag{27}$$

$$m_3 = \frac{|b|}{2}[(5 - 2\alpha\cos\phi_{ab} + P)^2 + (Q - 2\alpha\sin\phi_{ab})^2]^{1/2}, \tag{28}$$

where

$$P^2 = \frac{M \pm \sqrt{M^2 + N^2}}{2}, \qquad Q^2 = \frac{-M \pm \sqrt{M^2 + N^2}}{2}, \tag{29}$$

$$M = 25 + 4\alpha\cos\phi_{ab} + 4\alpha^2\cos 2\phi_{ab},$$
$$N = 4\alpha\sin\phi_{ab} + 4\alpha^2\sin 2\phi_{ab}. \tag{30}$$

Now, from Eqs. (23)–(25), we get the phases associated with the complex eigenvalues $m_{1,2,3}^c$. These phases can be written as $\gamma_i = \phi_b + \phi_i$, $i = 2, 3$. $i = 1$ is excluded here, as the lightest mass eigenvalue is zero, and the phase associated with m_1^c is $\gamma_1 = 0$. Now, $\phi_{2,3}$ in our model can be written as

$$\phi_2 = \tan^{-1}\left(\frac{Q + 2\alpha\sin\phi_{ab}}{5 - 2\alpha\cos\phi_{ab} - P}\right),$$
$$\phi_3 = \tan^{-1}\left(\frac{Q - 2\alpha\sin\phi_{ab}}{5 - 2\alpha\cos\phi_{ab} + P}\right). \tag{31}$$

Using the above relations, we can calculate the Majorana phase α_{32} in U_m, which can be written as

$$\alpha_{32} = \tan^{-1}\left(\frac{Q - 2\alpha\sin\phi_{ab}}{5 - 2\alpha\cos\phi_{ab} + P}\right) - \tan^{-1}\left(\frac{Q + 2\alpha\sin\phi_{ab}}{5 - 2\alpha\cos\phi_{ab} - P}\right). \tag{32}$$

The phase ϕ_b is irrelevant while calculating the Majorana phase, as it is the difference between γ_3 and γ_2. Finally, the Jarlskog invariant J_{CP} [96,97],

$$J_{CP} = \mathcal{I}(U_{11}U_{22}U_{12}^*U_{21}^*) = s_{12}c_{12}s_{13}c_{13}^2s_{23}c_{23}\sin\delta_{CP}, \tag{33}$$

will be used to quantify the CP violation in the FSS_1 model. From Eqs. (21)–(32), we observe that the mixing angles and all the phases depend on the parameters α and ϕ_{ab}, while the light neutrino masses depend on these parameters as well as on $|b|$. Now, we will estimate these model parameters (α, $|b|$, and ϕ_{ab}) using neutrino oscillation data on neutrino mixing angles and mass-squared differences. With measured values [23,98,99] of mixing angles θ_{13}, θ_{12}, and θ_{23}; mass-squared differences Δm_{21}^2, $|\Delta m_{31}^2|$ (mentioned in Eq. (1), taken from [23]); and the ratio r defined in Eq. (2), we first estimate α and the phase ϕ_{ab} using the 3σ range of neutrino oscillation data. The allowed ranges for α and ϕ_{ab} are plotted in the left panel of Fig. 1 in the $\alpha - \phi_{ab}$ plane. Here, we find that the allowed ranges of α vary between 4.82 and 5.27, whereas two distinct regions of ϕ_{ab} are allowed: 4.72–4.76 rad and 5.03–5.06 rad. As mentioned earlier, the effective light neutrino mass matrix in the FSS_1 model has rank 2 due to the considered A_4 symmetry. Hence, we obtain two massive light neutrinos as given in Eqs. (26)–(28), predicting *only* the normal ordering (NO) of light neutrino masses. To obtain the absolute values of m_2 and m_3, we need to find the overall factor $|b|$ appearing in Eqs. (27) and (28). Though the factor $|b|$ cancels out while calculating r, it can be calculated by fitting solar or atmospheric mass-squared differences after knowing α and ϕ_{ab} from the left panel of Fig. 1. After evaluating $|b|$, $|a|$ can be easily estimated using the relation $|a| = \alpha|b|$. Hence, in the right panel of Fig. 1, we have plotted the allowed region in the $|a| - |b|$ plane for the 3σ range of neutrino oscillation data. Corresponding to two distinct regions of ϕ_{ab} in the left panel, there also exist two distinct regions of the parameters $|a|$, as shown in the right panel of Fig. 1. Now, from Eqs. (27) and (28), we find that the light neutrino masses are functions of both a and b, whose origins lie in the type-I seesaw and the scotogenic contributions, respectively. Since $m_1 = 0$ in the FSS_1 framework, m_2 and m_3 are proportional to the solar and atmospheric mass-squared differences. Hence, in Fig. 2, we have plotted the variation of $|b|$ with respect to $|a|$ (represented by the color variation from blue to red) to reproduce correct r. This plot shows that the hierarchy between $|a|$ and $|b|$ essentially explains the observed value

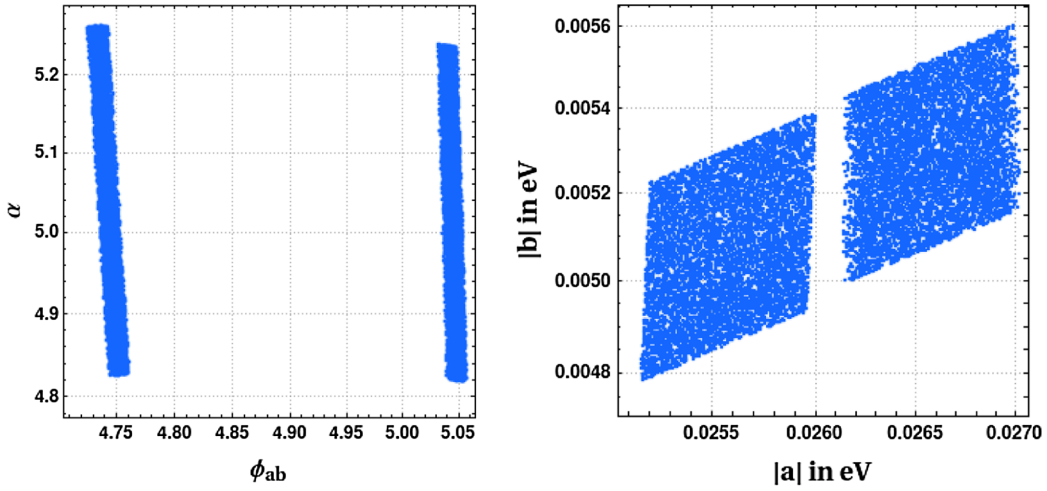

FIG. 1. The allowed regions for α and ϕ_{ab} (left panel), and $|a|$ and $|b|$ (right panel) for the 3σ ranges of neutrino oscillation data [23].

of the ratio of the solar to atmospheric mass-squared differences r, where $|a|$ is the dominant contribution originating from the type-I seesaw.

With the allowed values of α, ϕ_{ab}, $|a|$, and $|b|$ obtained from Fig. 1, we are in a position to study the correlations among neutrino mixing angles, phases, and masses. Due to the presence of the A_4 discrete flavor symmetry, we have realized the TM_1 mixing scheme yielding interesting correlations among the observables appearing in the neutrino mixing. It is well known that there are still some unsettled issues in the measurement of θ_{23} and δ_{CP} [23,98,99]. These are (i) the octant of θ_{23} (i.e., whether $\theta_{23} < 45°$ or $\theta_{23} > 45°$) and (ii) the precise measurement of δ_{CP}. Following Eqs. (21) and (22), we find a correlation between the atmospheric mixing angle θ_{23} and the Dirac CP phase δ_{CP} for the TM_1 mixing scheme. Together with Eq. (21) and Fig. 1 within the FSS_1 framework, the predictions regarding θ_{23} and δ_{CP} for the TM_1 scheme get constrained further, as plotted in the left panel of Fig. 3. Here, the gray-shaded region represents the TM_1 prediction in the $\theta_{23} - \delta_{CP}$ plane, where the red-shaded region is the prediction for the FSS_1 framework. We find that our model prefers the higher octant of θ_{23} for narrow regions of δ_{CP}. The allowed regions of $\sin^2\theta_{23}$ are 0.531–0.544 and 0.580–0.595, whereas the allowed regions of δ_{CP} are $\pm(1.44$–$1.12)$ rad. Here, the relative phase between type-I and scotogenic contributions (denoted by ϕ_{ab}) is the source of CP violation in the lepton sector—see Eq. (21) and subsequent discussion. Hence, in the right panel of Fig. 3, we have plotted the dependence of δ_{CP} on ϕ_{ab} (the relative phase between a and b) denoted by the red shaded regions. It is established that the Majorana phases cannot be constrained from neutrino oscillation data directly, as they do not appear in the neutrino oscillation probability [100–102]. In the FSS_1 framework, the Majorana phase α_{23} can be constrained using Eq. (32) with the allowed range for α and ϕ_{ab}. Hence, in the left panel of Fig. 4, we show the correlation among the CP phases in the $\alpha_{23} - \delta_{CP}$ plane, and the Majorana phase is found to be within the ranges 0.82–0.95 rad and 1.58–1.67 rad. Estimating the Majorana phase will play a crucial role in predicting the effective mass parameter appearing in the neutrinoless double decay [100]. Now, following Eq. (33), we have plotted the Jarlskog invariant J_{CP} as a function of ϕ_{ab} in the right panel of Fig. 4. Here, the magnitude of J_{CP} is found to be within the ranges 0.0290–0.0313 and 0.0318–0.0344. Finally, with the allowed parameter space obtained in Fig. 1, we make predictions for the light neutrino masses (m_2, m_3), their sum ($\sum m_i$), and the effective mass parameter appearing in the neutrinoless double decay ($m_{\beta\beta}$), as summarized in Table II. The prediction for $\sum m_i$ is consistent with cosmological observation [10],

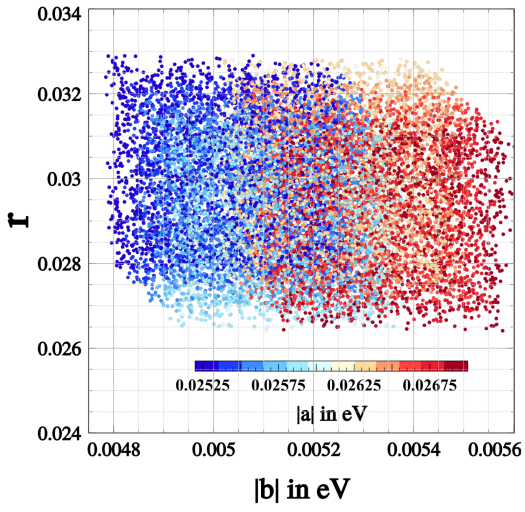

FIG. 2. r vs $|b|$ with variation of $|a|$.

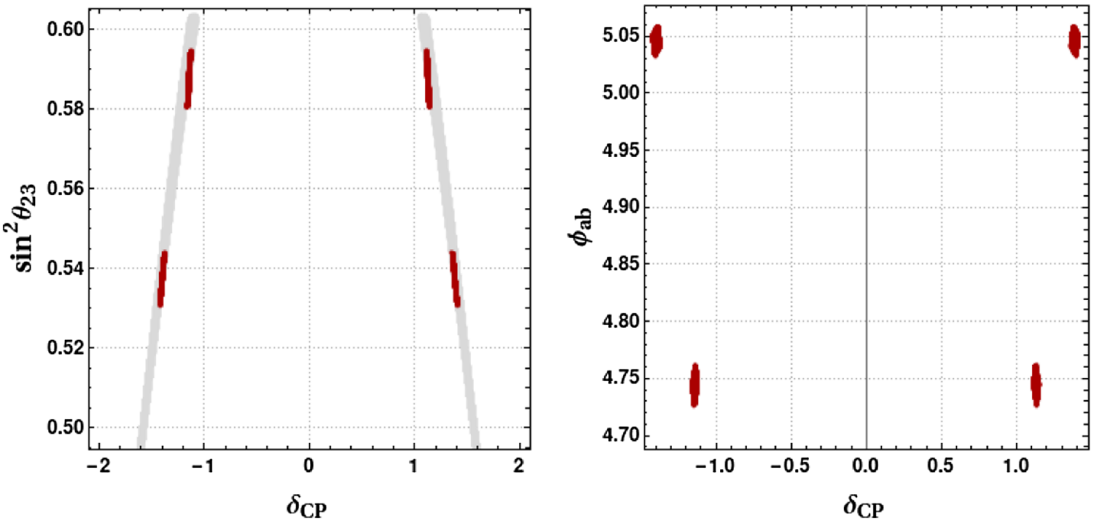

FIG. 3. $\sin^2\theta_{23} - \delta_{CP}$ correlation plot (denoted by red dots) is presented in the left panel. The gray-shaded region represents the generic prediction for the TM_1 mixing scheme. In the right panel, δ_{CP} is plotted against the relative (between a and b) phase factor ϕ_{ab}.

whereas the prediction for $m_{\beta\beta}$ falls below the upper limit provided by the next-generation double beta decay experiment nEXO [103].

V. SCALAR POTENTIAL

The FSS_1 model considered here consists of two $SU(2)$ doublet scalars, H and η. To obtain the flavor structure of the leptons, we have four flavons—ϕ_s, ϕ_a, ϕ_T, and ξ—as mentioned in Table I. These $SU(2)$ singlet flavons are considered to be very heavy compared to H and η and hence remain decoupled from the low-energy phenomenology of scalars. The low-energy scalar potential of the model can be written as

$$\begin{aligned} V = &-\mu_1^2(H^\dagger H) + \mu_2^2(\eta^\dagger\eta) + \lambda_1(H^\dagger H)^2 + \lambda_2(\eta^\dagger\eta)^2 \\ &+ \lambda_3(H^\dagger H)(\eta^\dagger\eta) + \lambda_4(H^\dagger\eta)(\eta^\dagger H) \\ &+ \frac{\lambda_5}{2}\{(H^\dagger\eta)(H^\dagger\eta) + \text{H.c.}\}. \end{aligned} \tag{34}$$

The doublets in the model can be parametrized as

$$\begin{aligned} H &= \begin{pmatrix} H^+ \\ v/\sqrt{2} + (h + i\zeta)/\sqrt{2} \end{pmatrix}, \\ \eta &= \begin{pmatrix} \eta^+ \\ (\eta_R + i\eta_I)/\sqrt{2} \end{pmatrix}. \end{aligned} \tag{35}$$

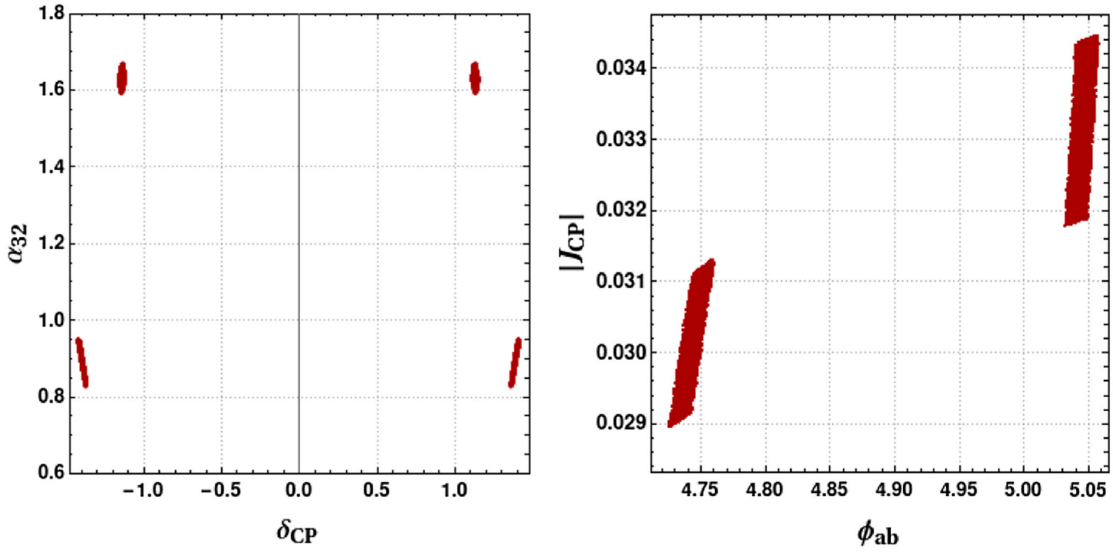

FIG. 4. Correlation plot between the Dirac CP phase δ_{CP} and the Majorana phase α_{32} (left panel); dependence of the Jarlskog invariant J_{CP} on ϕ_{ab} (right panel).

TABLE II. Predictions for m_2, m_3, $\sum m_i$, and $m_{\beta\beta}$ (all in meV) for the FSS_1 framework.

m_2	m_3	$\sum m_i$	$m_{\beta\beta}$
8.3–9.0	49.7–51.3	58.0–60.3	1.61–3.85

The electroweak gauge symmetry is given by

$$H = \begin{pmatrix} 0 \\ v/\sqrt{2} \end{pmatrix}, \qquad \eta = \begin{pmatrix} 0 \\ 0 \end{pmatrix}. \tag{36}$$

The above symmetry-breaking pattern ensures that the Z_2 symmetry will remain unbroken and results in two CP-even scalars (h, η_R) and one CP-odd neutral scalar η_I, in addition to a pair of charged scalars $(\eta^{\pm})$. Due to the dark Z_2 symmetry, there is no mixing between h and η_R, and h plays the role of the SM Higgs boson. The Z_2 symmetry also ensures the stability of the lightest scalar (η_R or η_I) that can act as a dark matter candidate. The masses of all scalars can be written in terms of the following parameters:

$$\{\mu_2, \lambda_1, \lambda_2, \lambda_3, \lambda_4, \lambda_5\}. \tag{37}$$

These parameters can be written in terms of physical masses of scalars as [104]

$$\lambda_1 = \frac{m_h^2}{2v^2}, \qquad \lambda_3 = \frac{2}{v^2}(M_{\eta^{\pm}}^2 - \mu_2^2), \tag{38}$$

$$\lambda_4 = \frac{M_{\eta_R}^2 + M_{\eta_I}^2 - 2M_{\eta^{\pm}}^2}{v^2}, \qquad \lambda_5 = \frac{M_{\eta_R}^2 - M_{\eta_I}^2}{v^2}. \tag{39}$$

We can choose all the λ's as free parameters—or, equivalently the four physical scalar masses, λ_2 and μ_2—namely

$$\{\mu_2^2, m_h, M_{\eta_R}, M_{\eta_I}, M_{\eta^{\pm}}, \lambda_2\}. \tag{40}$$

The quartic couplings are constrained theoretically by perturbativity and vacuum stability. We force the scalar potential to be perturbative, which requires all quartic couplings of the scalar potential to obey

$$|\lambda_i| \leq 8\pi. \tag{41}$$

To get the scalar potential to be bounded from below, the following conditions can be obtained [105,106]:

$$\lambda_{1,2} > 0 \quad \text{and} \quad \lambda_3 + \lambda_4 - |\lambda_5| + 2\sqrt{\lambda_1\lambda_2} > 0 \quad \text{and} \quad \lambda_3 + 2\sqrt{\lambda_1\lambda_2} > 0. \tag{42}$$

Equation (42) gives constraints based on the bare couplings of the Lagrangian. Another approach with running parameters of the model evaluated at the cutoff scale Λ of the theory is possible—see, for instance, Refs. [63,105–108]. Apart from these theoretical constraints, λ_3, λ_4, and λ_5 given in Eq. (39) can also be constrained from experimental and phenomenological constraints. As we will discuss in the subsequent sections, λ_5 is crucially relevant in determining the scotogenic Yukawa coupling and hence is constrained from DM relic density and direct-search constraints, as well as the neutrino phenomenology. Similarly, $\lambda_{3,4}$ can also be constrained from DM direct search, as well as SM Higgs diphoton signal strength.

The presence of the doublet scalar η in our model can have important consequences in the context of CDF-II W-boson mass anomaly [109] (for instance, see [110–117]), as it can affect the EW precision observables S, T, and U [95]. Through the self-energy correction of the W-boson with the doublet scalar in the loop, the W-boson mass can be increased from the SM prediction to the value obtained by the CDF-II Collaboration. Parametrizing the new physics effects in terms of the S, T, U parameters as [118,119], we find

$$\begin{aligned} S &= \frac{1}{12\pi}\ln\frac{M_{\eta^0}^2}{M_{\eta^+}^2}, \\ T &= \frac{G_F}{4\sqrt{2}\pi^2\alpha_{em}}\left(\frac{M_{\eta^0}^2 + M_{\eta^+}^2}{2} - \frac{M_{\eta^0}^2 M_{\eta^+}^2}{M_{\eta^0}^2 - M_{\eta^+}^2}\ln\frac{M_{\eta^+}^2}{M_{\eta^0}^2}\right), \\ U &= \frac{1}{12\pi}\left[\frac{(M_{\eta^0}^2 + M_{\eta^+}^2)(M_{\eta^0}^4 - 4M_{\eta^0}^2 M_{\eta^+}^2 + M_{\eta^+}^4)\ln(\frac{M_{\eta^+}^2}{M_{\eta^0}^2})}{(M_{\eta^+}^2 - M_{\eta^0}^2)^3} - \frac{5M_{\eta^0}^4 - 22M_{\eta^0}^2 M_{\eta^+}^2 + 5M_{\eta^+}^4}{3(M_{\eta^+}^2 - M_{\eta^0}^2)}\right], \end{aligned} \tag{43}$$

where $\eta_0 = (\eta_R + i\eta_I)/\sqrt{2}$, and the W-boson mass can be written as [120]

$$M_W^2 = (M_W^2)_{\rm SM} + \frac{\alpha_{em}\cos^2\theta_W}{\cos^2\theta_W - \sin^2\theta_W} M_Z^2 \left[-\frac{1}{2} S + \cos^2\theta_W T + \frac{(\cos^2\theta_W - \sin^2\theta_W)}{4\sin^2\theta_W} U \right], \tag{44}$$

where α_{em} is the fine structure constant, θ_W is the Weinberg angle, and $(M_W^2)_{\rm SM}$ is the SM predicted value of the W-boson mass. The dominant correction to M_W comes from the T parameter, which is very much sensitive to the mass difference between the charged scalar and the neutral scalar components of the inert doublet. And the CDF-II W mass can be obtained if the mass difference between η^+ and η_0 is around 80 to 100 GeV. However, we should stress that CDF-II data on the W mass are in contradiction with global electroweak e^+e^- fits and recent ATLAS LHC analysis, with systematic uncertainty improved by 15% [121] and optimized reconstruction of the W-boson transverse momentum [122].

VI. DM PHENOMENOLOGY FOR THE FSS_1 MODEL

In this FSS_1 framework, both type-I seesaw and scotogenic mechanisms are combined to obtain correct neutrino masses and mixing. The scotogenic contribution contains two potential candidates for DM: the lightest neutral scalar, and the singlet fermion. Determining the DM relic density hinges on these candidates' production mechanisms during the early Universe. While the literature extensively covers the scalar DM phenomenology,[4] which aligns with the inert doublet model (IDM) perspective, our focus here is on the singlet fermion denoted as f, an odd Z_2 particle in the scoto-seesaw scenario. We explore various mechanisms that can yield the correct relic density and delve into the associated parameter space. Since f is a gauge singlet, its production mechanism is intricately tied to its Yukawa couplings—see Eqs. (11) and (14)—with SM leptons and the inert doublet scalar η. The magnitude of these Yukawa couplings plays a pivotal role in determining whether the correct relic density can be achieved through thermal freeze-out or freeze-in mechanism.

A. Relic density of DM

As outlined in the preceding section, in our FSS_1 model, the scotogenic contribution to neutrino mass is parametrized in terms of the parameter b given in Eq. (14), which also plays a crucial role in explaining the observed neutrino oscillation data, which is constrained within in a range $|b| \in [0.0048, 0.0056]$ eV. Thus, to obtain the magnitude of Yukawa couplings that can satisfy this constraint with the masses of the loop particles of the order $\mathcal{O}(1\text{–}10^3)$ GeV,

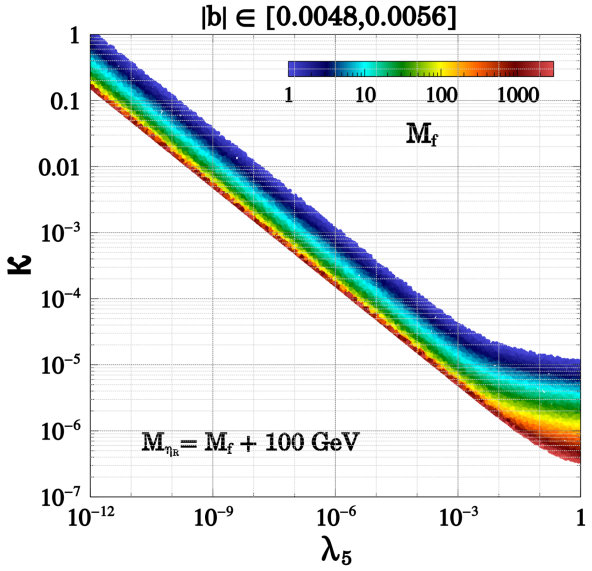

FIG. 5. Correlation between λ_5 defined in Eqs. (34) and (39), and κ defined in Eq. (14), consistent with the constraint from neutrino oscillation data—i.e., $|b| \in [0.0048, 0.0056]$ eV (see Fig. 1).

we perform a numerical scan, the result of which is shown in the plane of κ versus λ_5 in Fig. 5. We have used Eqs. (14) and (39) to obtain the estimations of κ and λ_5. It is worth noticing from the neutrino mass expression that in the limit $\lambda_5 \to 0$, the scotogenic contribution to neutrino mass vanishes. This is due to the fact that in this limit, the CP-even and CP-odd scalars η_R and η_I become degenerate, and thus $\mathcal{F}(M_{\eta_R}, M_{\eta_I}, M_f) \to 0$. Thus, to satisfy the constraints on b from neutrino oscillation data, if λ_5 is made small, then κ can be enhanced, and vice versa. We see that with this constraint on b, it is not possible to obtain Yukawa couplings smaller than $\mathcal{O}(10^{-6})$ even if λ_5 is $\mathcal{O}(1)$. Consequently, the singlet fermion also remains in thermal equilibrium with the SM bath. This equilibrium is guaranteed by the doublet scalar η, which, due to its gauge interactions, consistently maintains equilibrium with the SM bath during the early stages of the Universe. Hence, the DM relic density is governed through the WIMP mechanism. Several pertinent processes contribute to the relic density of DM. Specifically, the essential parameters influencing the relic density are the Yukawa couplings and the mass differences between the singlet fermion f and other particles in the dark sector, namely $\eta_{R,I}, \eta^\pm$.

For WIMP-type DM which is produced thermally in the early Universe, its thermal relic abundance can be obtained by solving the Boltzmann equation for the evolution of the DM number density,

$$\frac{dn}{dt} + 3Hn = -\langle\sigma v\rangle_{\rm eff}(n^2 - (n^{\rm eq})^2), \tag{45}$$

[4]For scalar dark matter phenomenology within the scoto-seesaw framework, see Ref. [63].

where $n = \sum_i n_i$ represents the total number density of all the dark sector particles, and $n^{\rm eq}$ is the equilibrium number density. $\langle\sigma v\rangle_{\rm eff}$ represents the effective annihilation cross section which takes into account all number-changing processes for DM freeze-out. It can be written as [123]

$$\begin{aligned}\langle\sigma v\rangle_{\rm eff} = &\frac{g_f^2}{g_{\rm eff}^2}\langle\sigma v\rangle_{ff} + \frac{g_f g_{\eta_R}}{g_{\rm eff}^2}\langle\sigma v\rangle_{f\eta_R}(1+\Delta_{\eta_R})^{3/2}\exp(-x\Delta_{\eta_R}) + \frac{g_f g_{\eta_I}}{g_{\rm eff}^2}\langle\sigma v\rangle_{f\eta_I}(1+\Delta_{\eta_I})^{3/2}\exp(-x\Delta_{\eta_I})\\
&+ \frac{g_f g_{\eta^\pm}}{g_{\rm eff}^2}\langle\sigma v\rangle_{f\eta^\pm}(1+\Delta_{\eta^\pm})^{3/2}\exp(-x\Delta_{\eta^\pm}) + \frac{g_{\eta_R}^2}{g_{\rm eff}^2}\langle\sigma v\rangle_{\eta_R\eta_R}(1+\Delta_{\eta_R})^{3}\exp(-2x\Delta_{\eta_R})\\
&+ \frac{g_{\eta_R} g_{\eta_I}}{g_{\rm eff}^2}\langle\sigma v\rangle_{\eta_R\eta_I}(1+\Delta_{\eta_R})^{3/2}(1+\Delta_{\eta_I})^{3/2}\exp\left(-x(\Delta_{\eta_R}+\Delta_{\eta_I})\right)\\
&+ \frac{g_{\eta_R} g_{\eta^\pm}}{g_{\rm eff}^2}\langle\sigma v\rangle_{\eta_R\eta^\pm}(1+\Delta_{\eta_R})^{3/2}(1+\Delta_{\eta^\pm})^{3/2}\exp\left(-x(\Delta_{\eta_R}+\Delta_{\eta^\pm})\right)\\
&+ \frac{g_{\eta_I}^2}{g_{\rm eff}^2}\langle\sigma v\rangle_{\eta_I\eta_I}(1+\Delta_{\eta_I})^{3}\exp(-2x\Delta_{\eta_I}) + \frac{g_{\eta^\pm}^2}{g_{\rm eff}^2}\langle\sigma v\rangle_{\eta^\pm\eta^\mp}(1+\Delta_{\eta^\pm})^{3}\exp(-2x\Delta_{\eta^\pm})\\
&+ \frac{g_{\eta_I} g_{\eta^\pm}}{g_{\rm eff}^2}\langle\sigma v\rangle_{\eta_I\eta^\pm}(1+\Delta_{\eta_I})^{3/2}(1+\Delta_{\eta^\pm})^{3/2}\exp(-x(\Delta_{\eta_I}+\Delta_{\eta^\pm})),\end{aligned} \tag{46}$$

where g_f, g_{η_R}, g_{η_I}, and $g_{\eta^\pm}$ represent the internal degrees of f, η_R, η_I, and $\eta^\pm$, respectively, and Δ_i stands for the ratio $(M_i - M_f)/M_f$, with M_i denoting masses of $\eta_R, \eta_I, \eta^\pm$. Here, $g_{\rm eff}$ is the effective degree of freedom, which is given by

$$\begin{aligned}g_{\rm eff} = &\, g_f + g_{\eta_R}(1+\Delta_{\eta_R})^{3/2}\exp(-x\Delta_{\eta_R})\\
&+ g_{\eta_I}(1+\Delta_{\eta_I})^{3/2}\exp(-x\Delta_{\eta_I})\\
&+ g_{\eta^\pm}(1+\Delta_{\eta^\pm})^{3/2}\exp(-x\Delta_{\eta^\pm}),\end{aligned} \tag{47}$$

and x is the dimensionless parameter M_f/T. The relic density of DM f can then be evaluated as

$$\Omega_f h^2 = \frac{1.09\times10^9\ {\rm GeV}^{-1}}{\sqrt{g_*}M_{\rm Pl}}\left[\int_{x_{\rm F.O.}}^{\infty} dx\,\frac{\langle\sigma v\rangle_{\rm eff}}{x^2}\right]^{-1}. \tag{48}$$

Here, $M_{\rm Pl}$ is the Planck mass, $x_{\rm F.O.} = M_f/T_{\rm F.O.}$, and $T_{\rm F.O.}$ denotes the freeze-out temperature of f. For this scenario, we have implemented the model in micrOMEGAs [124] to calculate the relic abundance of f. As is evident from Eq. (46), the mass difference between the dark sector particles—namely f and η, along with the coupling κ—is pivotal in determining the ultimate relic abundance of dark matter in this configuration. Smaller mass splittings can induce effective coannihilations between η and f, potentially reducing the relic abundance to the observed ballpark. The dominant number-changing processes relevant in governing the relic density are as shown in Figs. 6–8.

Clearly, the processes pivotal in establishing the relic abundance of dark matter fall into three distinct categories: (i) the annihilation of dark matter particles into both charged and neutral SM leptons (Fig. 6), (ii) the coannihilation of dark matter particles with scalar particles from the dark sector (Fig. 7), and (iii) the coannihilation contribution arising from the annihilation of dark sector scalars (Fig. 8). As denoted by Eq. (46), the coannihilation contribution to the effective annihilation cross section $\langle\sigma v\rangle_{\rm eff}$ is predominantly shaped by the mass difference between dark matter and the dark scalars.

To elucidate the influence of Yukawa couplings and mass splitting on the relic abundance of dark matter, in Fig. 9, we illustrate the variation of relic density with the dark matter mass. In the left panel of Fig. 9, the Yukawa coupling κ is varied within the range $\kappa \in [10^{-4}, 10^{-3}]$, while the mass difference between the lightest neutral scalar η_R and f (i.e., $M_{\eta_R} - M_f$) is varied in three different ranges, as indicated in the figure's inset. Evidently, an increase in the mass difference leads to a corresponding increase in the relic density. This trend arises because the coannihilation contribution to $\langle\sigma v\rangle_{\rm eff}$ gradually diminishes with an increase in $(M_{\eta_R} - M_f)$, thereby boosting the relic abundance of f.

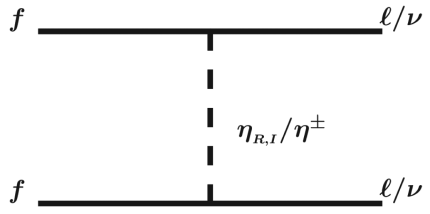

FIG. 6. Annihilations of dark matter into SM leptons.

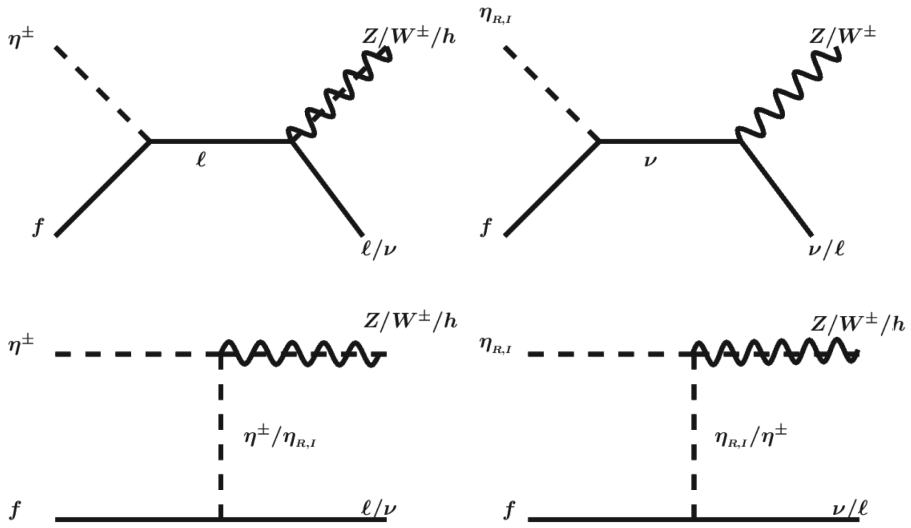

FIG. 7. Coannihilations among dark matter and other dark sector particles.

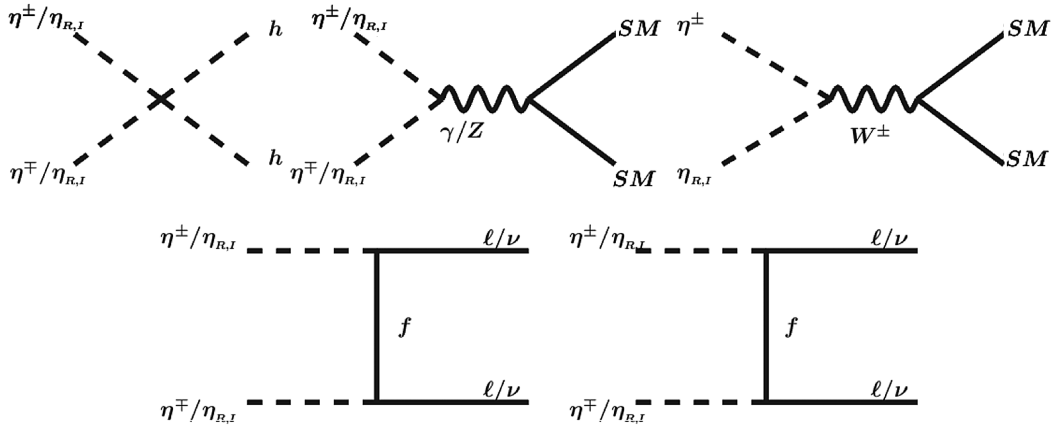

FIG. 8. Annihilations of scalar coannihilation partners.

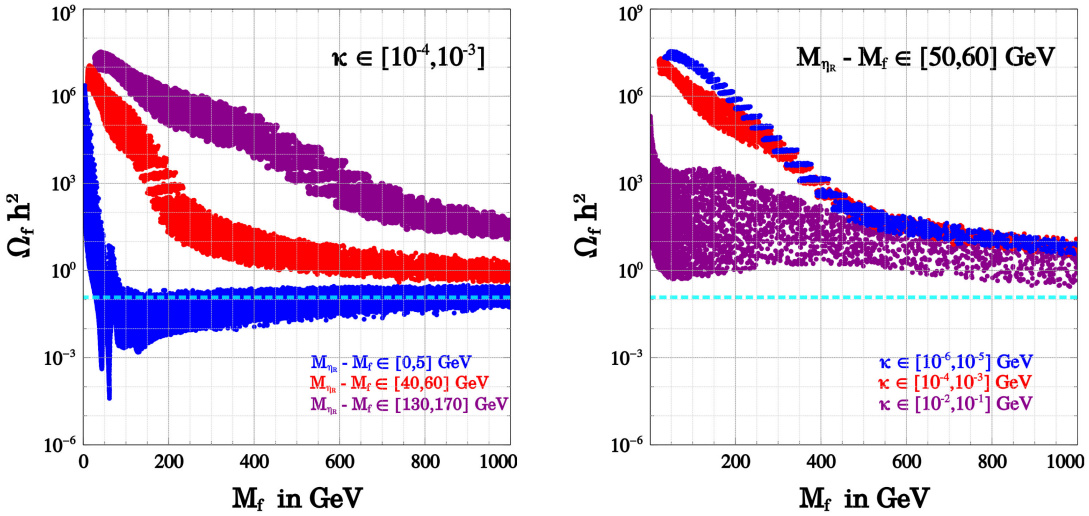

FIG. 9. DM relic density as a function of DM mass with the Yukawa couplings (left panel) and mass difference $M_{\eta_R} - M_f$ (right panel) varied randomly as mentioned in the inset of the figure. The horizontal cyan line represents the observed relic density [52].

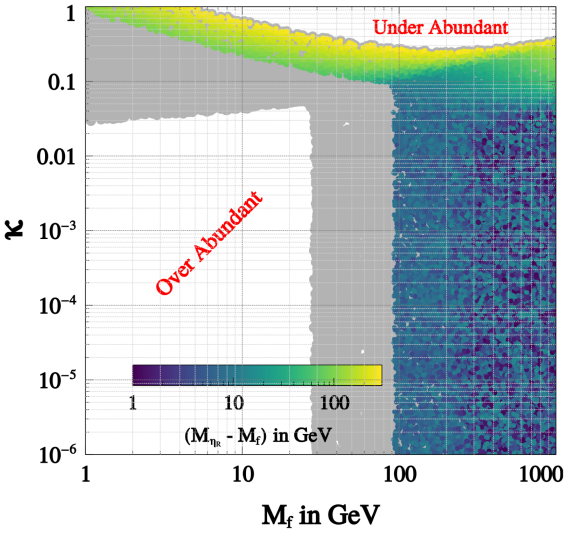

FIG. 10. Correct relic-density-satisfying points in the plane of DM mass M_f and κ. The color code shows the value of $M_{\eta_R} - M_f$.

Expanding the analysis, in the right panel of Fig. 9, the mass difference $(M_{\eta_R} - M_f)$ is varied within a small range of [50, 60] GeV, and the variation of relic density with dark matter mass is then showcased for three different ranges of Yukawa couplings, as outlined in the figure's inset. It is evident that an increase in Yukawa coupling leads to a decrease in relic density, attributed to the increase in $\langle \sigma v \rangle_{\text{eff}}$. Additionally, an intriguing observation from this figure is that, when $(M_{\eta_R} - M_f) \in [50, 60]$ GeV and Yukawa couplings are small [i.e., $\kappa \lesssim \mathcal{O}(10^{-3})$], the relic density does not change with further reduction in Yukawa couplings for dark matter masses exceeding 500 GeV, as indicated by the red- and blue-colored points. This phenomenon can be explained by the fact that, in scenarios with small Yukawa couplings, neither the annihilation of DM nor the coannihilation of DM with dark sector scalars efficiently affects the relic density. Instead, it is primarily determined by the coannihilation contribution from the annihilation of dark scalar partners. Conversely, in situations where Yukawa couplings are large and the mass difference is substantial, the relic density is primarily influenced by the annihilation of DM, as indicated by the purple-colored points.

Thus, in summary of the effects that affect the relic density, in scenarios characterized by small Yukawa couplings and substantial mass differences (Δ_i), the relic density is predominantly governed by the coannihilation contribution from the dark scalars. In such scenarios, DM annihilation becomes subdominant, and coannihilation among dark matter and dark scalars is suppressed due to the large mass splitting. Conversely, when the mass difference between dark matter and dark scalars is not considerably large, coannihilation among DM and dark scalars, as well as dark scalar annihilations, plays a crucial role in determining the relic density. Only in cases where Yukawa couplings are significantly large and the mass difference is also substantial do dark matter annihilations become relevant for achieving the correct relic density.

We present the parameter-space-satisfying correct relic density in the plane of M_f and κ, with the color code representing the corresponding value of $M_{\eta_R} - M_f$, in Fig. 10. The gray-colored points are ruled out by imposing a conservative limit on the doublet scalar mass given by the LEP experiment of about $M_\eta \geq 100$ GeV. It is evident that, when the DM mass is small and κ is small, the effective annihilation cross section is very small, and thus it is not possible to achieve correct relic density even with coannihilation contributions. Thus, we obtain an overabundant region below M_f around 30 GeV and $\kappa \lesssim \mathcal{O}(10^{-2})$. In the small-DM-mass range $M_f \lesssim 100$ GeV, the correct relic density can be obtained only when the Yukawa couplings are significant—i.e., $\kappa \sim \mathcal{O}(1)$—such that the DM annihilation cross section is appropriate to match the thermal cross section, as in this region the coannihilation contributions are negligible. When the DM mass is greater than 100 GeV, and the Yukawa coupling $\kappa \lesssim \mathcal{O}(10^{-2})$, we see that with an increase in DM mass, the value of $M_{\eta_R} - M_f$ shows a gradual decrease to achieve the correct relic density. This is attributed to the fact that as the DM mass increases, the effective cross section gradually decreases, thereby increasing the relic density, and thus it needs more effective coannihilations, which are made possible by decreasing $M_{\eta_R} - M_f$ to bring the relic density within the correct ballpark. We also observe an underabundant region when $\kappa \gtrsim \mathcal{O}(10^{-1})$, even with very large $M_{\eta_R} - M_f$. This is due to the fact that, with very large κ, the DM annihilation cross section is large. So even if the coannihilation contribution is suppressed because of large $M_{\eta_R} - M_f$, it is still not possible to achieve the correct density.

B. Direct detection of DM

As the sole interaction connecting f with SM particles is the Yukawa term in Eq. (8), direct interactions between quarks and dark matter are absent at the tree level. However, at the one-loop level, f can have effective couplings with various SM particles, such as the photon, Z boson, and Higgs boson. Specifically, the exchange of the Z-boson results in the emergence of an effective axial vector interaction, which gives rise to a spin-dependent DM-nucleon scattering and is dominant only when the couplings between Higgs and η are very small. The constraints of spin-dependent DM nucleon scattering is also relatively less constrained as compared to the spin-independent scattering cross sections. Thus, we focus here on the spin-independent DM-nucleon scattering rate, as the direct-search experiments very stringently constrain it. The detection rate of dark matter particles within a detector can experience an

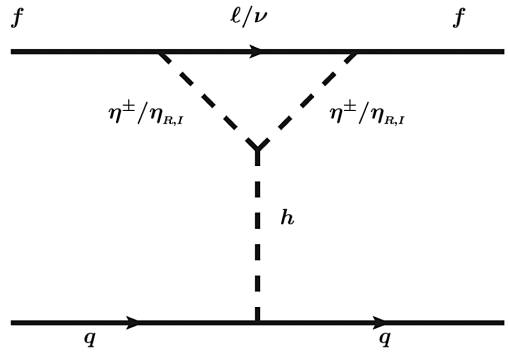

FIG. 11. Spin-independent elastic DM-nucleon scattering arising at one loop.

amplification if the quartic couplings λ_3 and λ_4 are significant. When this condition is met, the exchange of Higgs bosons, as depicted in Fig. 11, leads to the emergence of an effective scalar interaction term between the quark q and the dark matter particle f. This interaction is effectively described by $S_q \bar{q} q \bar{f} f$, where

$$S_q = -\frac{\kappa^2}{16\pi^2 M_h^2 M_f}\left[\lambda_3 \mathcal{G}\left(\frac{M_f^2}{M_{\eta^\pm}^2}\right) + \frac{(\lambda_3+\lambda_4)}{2}\mathcal{G}\left(\frac{M_f^2}{M_0^2}\right)\right], \tag{49}$$

with the loop function $\mathcal{G}(x)$ defined as

$$\mathcal{G}_1(x) = \frac{x + (1-x)\ln(1-x)}{x}, \tag{50}$$

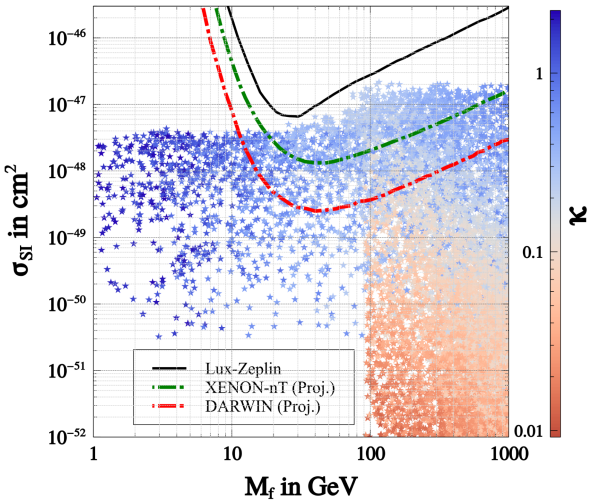

FIG. 12. Spin-independent DM-nucleon scattering cross section as a function of DM mass for the points satisfying correct relic density. The color code represents the value of κ. The black solid line represents the most recent constraint from the Lux-Zeplin experiment. The green and red dot-dashed lines represent the projected sensitivities of the XENON-nT and DARWIN experiments, respectively.

and its value spans between 0 and 1 for $0 \le x \le 1$. This interaction then results in the computation of the spin-independent cross section $\sigma_{\rm SI}$ for the interaction of f with a proton, and the expression for $\sigma_{\rm SI}$ is given by

$$\sigma_{\rm SI} = \frac{4}{\pi}\frac{M_f^2 m_p^2}{(M_f+m_p)^2} m_p^2 S_q^2 f_p^2, \tag{51}$$

where f_p represents the scalar form factor. We show the DM-nucleon scattering cross section as a function of DM mass for the points satisfying correct relic density in Fig. 12. Because of the loop suppression, we observe that even when the Yukawas and scalar quartic couplings are large, none of the points are ruled out, and the parameter space remains safe from the DM direct-search constraints. However, interestingly, future experiments like XENON-nT [125] and DARWIN [126] with enhanced sensitivity can probe the Yukawa coupling κ down to $\mathcal{O}(0.1)$.

VII. HIGGS BOSON IN THE DIPHOTON DECAY CHANNEL

The SM Higgs boson has a mass of $m_h \simeq 125$ GeV [84,127], and one of the main decay channels is the diphoton, where the SM rate for $h \to \gamma\gamma$ is dominated by the W-boson loop contribution. The signal strength of $h \to \gamma\gamma$ is the ratio between the observed cross section $pp \to h \to \gamma\gamma$ and the same quantity computed in the SM. The observed cross section $pp \to h \to \gamma\gamma$ should match the FSS_1 model prediction. Since the dominant process of the Higgs boson production is gluon fusion, in the first approximation, the production cross section of the Higgs boson in the FSS_1 model is the same as in the SM. As a result, following [104], after using narrow-width approximation, the signal strength of $h \to \gamma\gamma$ in the model can be written as

$$\begin{aligned} R_{\gamma\gamma} &= \frac{[\sigma(gg \to h) \times \mathrm{Br}(h \to \gamma\gamma)]_{\mathrm{FSS}_1}}{[\sigma(gg \to h) \times \mathrm{Br}(h \to \gamma\gamma)]_{\mathrm{SM}}} \\ &= \frac{\Gamma^h_{\mathrm{SM}}}{\Gamma^h_{\mathrm{FSS}_1}} \frac{\Gamma(h \to \gamma\gamma)_{\mathrm{FSS}_1}}{\Gamma(h \to \gamma\gamma)_{\mathrm{SM}}}. \end{aligned} \tag{52}$$

Here, the quantities with the FSS_1 and SM suffixes are computed in the flavored scoto-seesaw and the Standard Model, respectively. $\Gamma^h_{\mathrm{FSS}_1,\mathrm{SM}}$ is the total decay width for these models. The $h \to \gamma\gamma$ decay is experimentally well established, and in the LHC, the signal strength of $h \to \gamma\gamma$ is $R = 1.04^{+0.10}_{-0.09}$ [84]. While computing $R_{\gamma\gamma}$, we take for the total decay width of the Higgs boson $\Gamma^h_{\mathrm{SM}} = 4.07 \times 10^{-3}$ GeV with a relative uncertainty of $^{+4.0\%}_{-3.9\%}$ [95]. For a theoretical error estimate, see also [128]. For detailed studies on $h \to \gamma\gamma$ decays within miscellaneous beyond-SM scenarios, see [104,129–132]. In the framework of the FSS_1 model, this decay can be enhanced with the charged

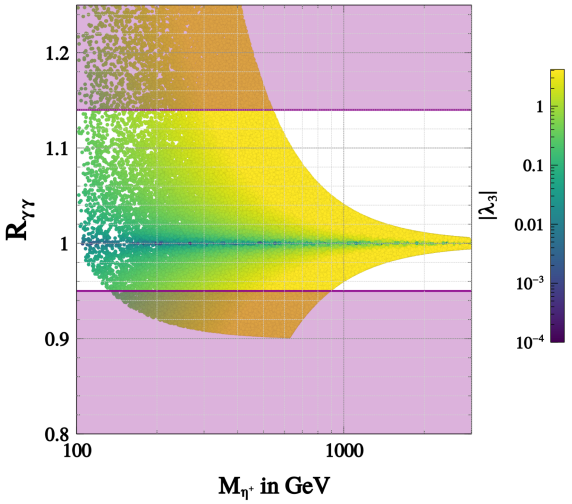

FIG. 13. $R_{\gamma\gamma}$ is plotted against m_{η^+} in the plane of λ_3. The white-shaded region is the allowed region determined by the ATLAS experiment [84].

scalars ($\eta^{\pm}$) in the loop, over the SM contribution with charged fermions and W bosons in the loop. Using Eq. (52), the expression for the partial decay width of $h \to \gamma\gamma$ in the FSS_1 model induced by the $\eta^{\pm}$ loop can be written as [133]

$$\Gamma(h \to \gamma\gamma) = \frac{G_F \alpha_{em}^3 m_h^3}{128\sqrt{2}\pi^3}\left|\sum_f N_f Q_f^2 F_{1/2}(\beta_f) + F_1(\beta_W) + \frac{\lambda_3 v^2}{2M_{\eta^+}^2} F_0(\beta_{\eta^{\pm}})\right|^2, \tag{53}$$

where $\beta_i = 4M_i^2/m_h^2$, $i = f, W, \eta^+$. N_f is the color factor, and Q_f is the charge of quarks. α_{em} and G_F are the fine structure constant and the Fermi constant. The F functions in Eq. (53) are the form factors of spin-1/2, 1, and 0 fields for the $h \to \gamma\gamma$ decay:

$$F_{1/2}(\beta_f) = -2\beta[1 + (1-\beta)f(\beta)], \tag{54}$$

$$F_1(\beta_W) = [2 + 3\beta + 3\beta(2-\beta)f(\beta)], \tag{55}$$

$$F_0(\beta_{\eta^{\pm}}) = \beta[1 - \beta f(\beta)], \tag{56}$$

where

$$f(\beta) = \left(\sin^{-1}\frac{1}{\sqrt{\beta}}\right)^2, \qquad \beta \geq 1 \tag{57}$$

$$= -\frac{1}{4}\left[\ln\frac{1+\sqrt{1-\beta}}{1-\sqrt{1-\beta}} - i\pi\right]^2, \qquad \beta < 1. \tag{58}$$

In the FSS_1 model, therefore, the total decay width of the Higgs boson can be written as

$$\Gamma^{h}_{\mathrm{FSS}_1} = \Gamma^{h}_{\mathrm{SM}} + \Gamma(h \to \eta_R\eta_R) + \Gamma(h \to \eta_I\eta_I) + \Gamma(h \to \eta^+\eta^-). \tag{59}$$

In the above equation, the decay width of the Higgs boson to different scalar particles is calculated using tree-level couplings:

$$\lambda_{h\eta_R\eta_R} = \frac{2}{v}(M_{\eta_R}^2 - \mu_2^2), \tag{60}$$

$$\lambda_{h\eta_I\eta_I} = \frac{2}{v}(M_{\eta_I}^2 - \mu_2^2). \tag{61}$$

Doing numerical analysis for $\Gamma(h \to \gamma\gamma)$, we scan the parameters of the FSS_1 model in the range

$$100\ \mathrm{GeV} < M_{\eta_R}, M_{\eta_I}, M_{\eta^+} < 2000\ \mathrm{GeV}, \qquad |\lambda_{3,4,5}| \leq 4\pi. \tag{62}$$

In Eq. (59), the total decay width of SM Higgs h in the FSS_1 model has three extra contributions over the SM. In the FSS_1 framework, the scalars η_R and η_I are not the lightest neutral Z_2-odd particles of the theory, f being the DM candidate. Thus, with a judicious choice of the DM mass M_f (satisfying relic density and direct-search constraints), the Higgs boson decays to $\eta_R\eta_R$ and $\eta_I\eta_I$ can be made kinematically forbidden. The result of numerical analysis is shown in Fig. 13, where the signal strength of $R_{\gamma\gamma}$ in the wide λ_3 range is given as a function of the charged scalar mass M_{η^+}. The horizontal white region ($R_{\gamma\gamma} = 1.04^{+0.10}_{-0.09}$) represents the currently allowed region measured by the ATLAS experiment using 139 fb^{-1} of pp collision data at $\sqrt{s} = 13$ TeV [84]. This shows that the M_{η^+} masses heavier than 1000 GeV are completely safe from LHC constraints. As follows from Eq. (53), if $\lambda_3 < 0$, the partial decay width of h is smaller than in the SM, while positive λ_3 will give an enhancement beyond the SM value. So, depending on the positive or negative value of λ_3, we get $R_{\gamma\gamma} > 1$ or $R_{\gamma\gamma} < 1$, respectively. This behavior can be seen in Fig. 13.

VIII. LEPTON FLAVOR VIOLATION

The constraints on lepton-flavor-violating (LFV) processes are an important aspect of the FSS_1 model under consideration. The model offers specific predictions, given that the flavor structure of the Yukawa couplings is entirely dictated by the A_4 discrete flavor symmetry and the alignment of flavon vacuums. Along with neutrino masses, mixing, and DM phenomenology, LFV decays also give valuable insight on the FSS_1 model parameters. As a consequence of the considered flavor symmetry, the Yukawa couplings in the charged lepton sector are diagonal; see Eq. (7). However, the Yukawa couplings y_N and y_s in Eq. (8), associated with the type-I seesaw and scotogenic

mechanisms, respectively, contribute to the LFV decays. These Yukawa couplings can generate lepton-flavor-violating processes[5] like $l_\alpha \to l_\beta\gamma$ and $l_\alpha \to 3l_\beta$ ($\alpha,\beta = e, \mu, \tau$). Studies on these LFV decays completely depend on the FSS_1 model construction as described below.

In our framework, the branching ratios of the $l_\alpha \to l_\beta\gamma$ decays for the scotogenic contribution can be written as [61,134]

$$\mathrm{Br}(l_\alpha \to l_\beta\gamma) \approx \frac{3\pi\alpha_{em}}{64G_F^2}|Y_F^{\beta*}Y_F^{\alpha}|^2\frac{1}{M_{\eta^+}^4}\left(F_1\left(\frac{M_f^2}{M_{\eta^+}^2}\right)\right)^2 \times \mathrm{Br}(l_\alpha \to l_\beta\nu_\alpha\bar{\nu}_\beta). \tag{63}$$

Here, G_F is the Fermi constant, and Y_F is the Yukawa coupling matrix from the scotogenic contribution given in Eq. (11). The expression for the function F_1 is given by

$$F_1(x) = \frac{1-6x+3x^2+2x^3-6x^2\log x}{6(1-x)^4}. \tag{64}$$

As mentioned earlier, the Yukawa couplings are determined by the considered discrete symmetries of the model. Due to the specific VEV structure of the A_4 triplet flavon, $Y_F^\tau = 0$ as given in Eq. (11). Therefore, the scotogenic contribution alone yields a vanishing contribution for $\tau \to e\gamma$ and $\tau \to \mu\gamma$ lepton-flavor-violating decays. So, the only nonvanishing contribution arising in the decays of the form $l_\alpha \to l_\beta\gamma$ comes from the $\mu \to e\gamma$ decay, with its branching fraction given by [61,134]

$$\mathrm{Br}(\mu \to e\gamma) \approx \frac{3\pi\alpha_{em}}{64G_F^2}|2y_s y_s^*\epsilon^4|^2\frac{1}{M_{\eta^+}^4}\left(F_1\left(\frac{M_f^2}{M_{\eta^+}^2}\right)\right)^2 \times \mathrm{Br}(\mu \to e\nu_\mu\bar{\nu}_e) \tag{65}$$

$$= \frac{3\pi\alpha_{em}}{16G_F^2M_f^2}\left(\frac{|b|}{\mathcal{F}(M_{\eta_R},M_{\eta_I},M_f)}\right)^2\frac{1}{M_{\eta^+}^4}\left(F_1\left(\frac{M_f^2}{M_{\eta^+}^2}\right)\right)^2 \times \mathrm{Br}(\mu \to e\nu_\mu\bar{\nu}_e), \tag{66}$$

where we have substituted Eq. (11) into Eq. (65) to obtain Eq. (66). In the above, $\epsilon = v_f/\Lambda$, where for simplicity we have assumed all flavon VEVs to be the same—i.e., $v_\xi = v_{s,a} = v_f$. Clearly, $\mathrm{Br}(\mu \to e\gamma)$ depends on the parameter $|b|$, which is constrained from neutrino oscillation data ranging from 0.0048 to 0.0056 eV, as given in Fig. 1. Another type of LFV decays appearing in our FSS_1 framework are the $l_\alpha \to 3l_\beta$ ($l_\alpha \to l_\beta\bar{l}_\beta l_\beta$) processes. The corresponding branching ratios are given by [134]

$$\mathrm{Br}(l_\alpha \to 3l_\beta) \approx \frac{3\alpha_{em}{}^2}{512G_F^2}|Y_F^{\beta*}Y_F^{\alpha}|^2\frac{1}{M_{\eta^+}^4}\mathcal{G}\left(\frac{m_\alpha}{m_\beta}\right)\left(F_2\left(\frac{M_f^2}{M_{\eta^+}^2}\right)\right)^2 \times \mathrm{Br}(l_\alpha \to l_\beta\nu_\alpha\bar{\nu}_\beta), \tag{67}$$

where

$$F_2(x) = \frac{2-9x+18x^2-11x^3+6x^3\log x}{6(1-x)^4}, \tag{68}$$

$$\mathcal{G}\left(\frac{m_\alpha}{m_\beta}\right) = \left(\frac{16}{3}\log\left(\frac{m_\alpha}{m_\beta}\right) - \frac{22}{3}\right). \tag{69}$$

Again, following Eq. (11), we find that $Y_F^\tau = 0$, hence the branching fractions for $\tau \to 3e$ and $\tau \to 3\mu$ decays vanish. The only nonvanishing contribution originates from the $\mu \to 3e$ decay, and its branching fraction can be written as [134]

$$\mathrm{Br}(\mu \to 3e) \approx \frac{3\alpha_{em}{}^2}{512G_F^2}|2y_s y_s^*\epsilon^4|^2\frac{1}{M_{\eta^+}^4}\mathcal{G}\left(\frac{m_\mu}{m_e}\right) \times \left(F_2\left(\frac{M_f^2}{M_{\eta^+}^2}\right)\right)^2, \tag{70}$$

$$= \frac{3\alpha_{em}^2}{128M_f^2G_F^2}\left(\frac{|b|}{\mathcal{F}(M_{\eta_R},M_{\eta_I},M_f)}\right)^2\frac{1}{M_{\eta^+}^4}\mathcal{G}\left(\frac{m_\mu}{m_e}\right) \times \left(F_2\left(\frac{M_f^2}{M_{\eta^+}^2}\right)\right)^2, \tag{71}$$

where we have substituted Eq. (11) into Eq. (70) to obtain Eq. (71) with $\epsilon = v_f/\Lambda$. Similarly to Eq. (66), here we also find that $\mathrm{Br}(\mu \to 3e)$ depends on the scotogenic mass parameters $M_{f,\eta^+,\eta_R,\eta_I}$ as well as $|b|$, the parameter involved in explaining the correct neutrino oscillation parameter and DM relic density. The variation of the corresponding coupling λ_5 is given in the inset. In Fig. 14, we have shown plots for $\mu \to e\gamma$ (left panel) and $\mu \to 3e$ (right panel) branching ratios against the dark matter mass M_f, satisfying the bound on $|b|$ obtained from Fig. 1. The current constraint (denoted by a red line) for the branching ratio of the $\mu \to e\gamma$ decay is given by the MEG-II experiment as $\mathrm{Br}(\mu \to e\gamma) \le 3.1 \times 10^{-13}$ [137], whereas for $\mu \to 3e$ decay the constraint by the SINDRUM experiment is given as $\mathrm{Br}(\mu \to 3e) \le 1 \times 10^{-12}$ [138]. In both plots, a current upper bound on both these decays constrains the dark matter mass M_f specifically in the low-mass region. M_f will be further constrained by the future MEG-II (Proj.) [139] and Mu3e Phase-I [140] experiments. To illustrate the dependence of the LFV branching ratio on the neutrino oscillation parameters and its consistency with the DM phenomenology, in Fig. 15, we have plotted $\mathrm{Br}(\mu \to e\gamma)$

[5]To study lepton flavor violation in the pure scotogenic model, see Refs. [134–136].

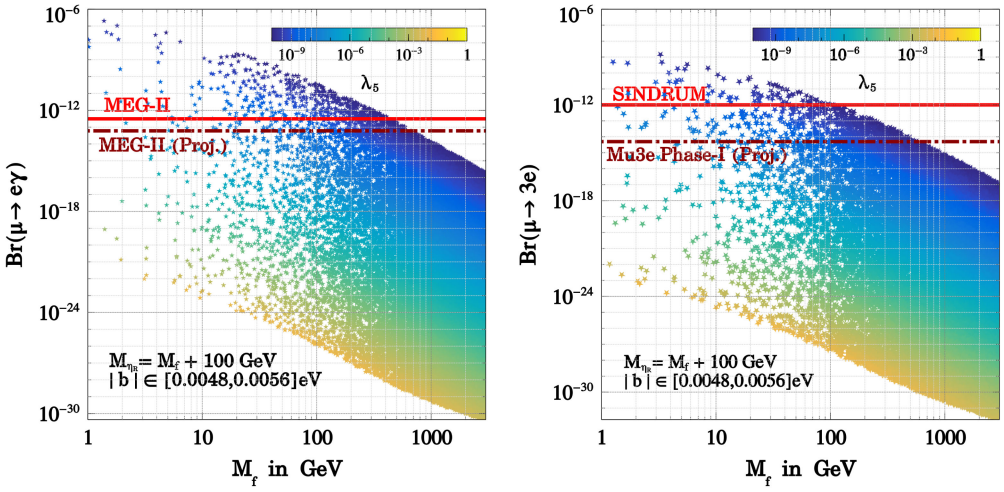

FIG. 14. The branching ratio of $\mu \to e\gamma$ ($\mu \to 3e$) is plotted against the dark matter mass M_f in the left (right) panel. In both panels, the red line corresponds to the present upper bound, and the brown line corresponds to the future sensitivity (see text for details).

against $|b|$. Here, the white-shaded region is consistent with correct neutrino masses and the mixing given in the right panel of Fig. 1. Hence, the cyan-shaded regions are ruled out by neutrino oscillation data. This plot also depicts the dependence of the branching ratio on the scotogenic Yukawa coupling shown by the variation of κ. The upper shaded region is already ruled out by the recent updated constraint from MEG-II [137], and the projected sensitivity of MEG-II can probe κ of the order $\mathcal{O}(10^{-2})$.

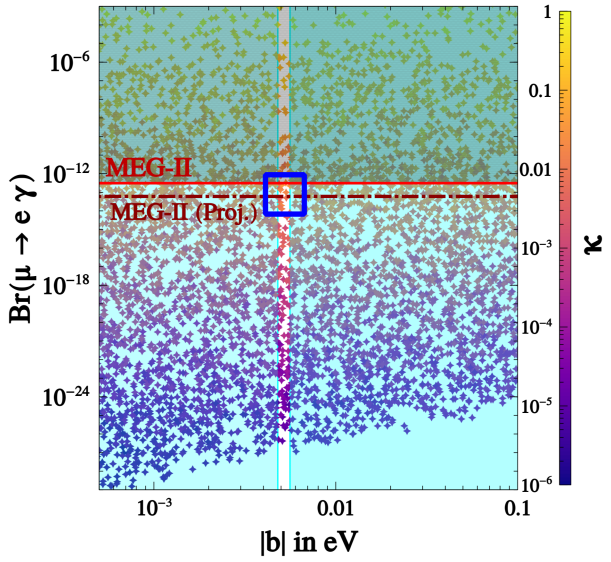

FIG. 15. The branching ratio for $\mu \to e\gamma$ is plotted against $|b|$ for the points satisfying correct relic density of DM. The variation of color legends is for the variation of κ. Cyan-shaded regions rule out values of $|b|$ other than those consistent with the neutrino oscillation data: (0.0048–0.0056) eV. Solid red and dot-dashed brown lines represent the recent updated constraint from MEG-II and its projected sensitivity, respectively.

For the type-I seesaw contributions to LFV decays, the branching fractions for $l_\alpha \to l_\beta\gamma$ decays can be cast in the following form:

$$\mathrm{Br}(l_\alpha \to l_\beta\gamma) \approx \frac{3\alpha_{em}v^4}{8\pi M_N^4}\left|Y_N^\beta Y_N^{\alpha^*} f\left(\frac{M_N^2}{M_W^2}\right)\right|^2, \tag{72}$$

where Y_N is given in Eq. (10). The loop function $f(x)$ in Eq. (72) is

$$f(x) = \frac{x(2x^3+3x^2-6x-6x^2\log(x)+1)}{2(1-x)^4}. \tag{73}$$

Similarly to the scotogenic contribution, the A_4 discrete symmetry and the VEV alignment of the flavon ϕ_s play a crucial role in estimating the branching ratio for $l_\alpha \to l_\beta\gamma$. The VEV alignment of the flavon ϕ_s is such that it gives $Y_N^e = 0$, as a result of which the branching fractions for $\mu \to e\gamma$ and $\tau \to e\gamma$ decays vanish. The only nonvanishing contribution arising in the type of $l_\alpha \to l_\beta\gamma$ decay is $\tau \to \mu\gamma$, and the branching fraction is given by

$$\begin{aligned}\mathrm{Br}(\tau \to \mu\gamma) &= \frac{3\alpha_{em}v^4}{8\pi M_N^4}\left|(y_N y_N^* \epsilon^2 f\left(\frac{M_N^2}{M_W^2}\right)\right|^2 \\ &= \frac{3\alpha_{em}}{8\pi M_N^2}|a|^2\left|f\left(\frac{M_N^2}{M_W^2}\right)\right|^2.\end{aligned} \tag{74}$$

For $M_N \sim 10^4$ GeV and $|a| = 0.0250$ eV, the branching fraction in Eq. (74) gives 5.4×10^{-33}, which is very small compared to the experimental limit (4.4×10^{-8}) [141]. For higher M_N values, the branching ratio will be even more suppressed. Similarly, the branching ratio for the $\tau \to 3\mu$ conversion is found to be very small compared to the experimental bound [142].

TABLE III. Possible lepton-flavor-violating decay modes and their origin in the FSS_1 framework. The ✓ and ✗ symbols stand for allowed and disallowed regimes.

Decay modes	Scotogenic	Seesaw	Remarks
$\mu \to e\gamma$	✓	✗	$Y_N^e = 0$
$\tau \to e\gamma$	✗	✗	$Y_F^\tau = 0, Y_N^e = 0$
$\tau \to \mu\gamma$	✗	✓	$Y_F^\tau = 0$
$\mu \to 3e$	✓	✗	$Y_N^e = 0$
$\tau \to 3e$	✗	✗	$Y_F^\tau = 0, Y_N^e = 0$
$\tau \to 3\mu$	✗	✓	$Y_F^\tau = 0$

In Table III, we have summarized the allowed LFV decays in the FSS_1 model. The considered discrete flavor symmetry and corresponding vacuum alignment of the flavons completely disallow decay channels such as $\tau \to e\gamma$ and $\tau \to 3e$. Such a decisive prediction can be made since we have vanishing values for the Yukawa couplings Y_F^τ and Y_N^e—see Eqs. (10) and (11)—associated with the scotogenic and type-I seesaw contributions, respectively. Present experiments already exclude branching ratios larger than about $\mathcal{O}(10^{-8})$. Any positive signal by the future experiments will essentially test the validity of the FSS_1 framework.

IX. SUMMARY OF PHENOMENOLOGICAL ANALYSIS

Both the type-I seesaw and the scotogenic contribution within our FSS_1 framework are crucial in explaining the hierarchy associated with the neutrino mass-squared differences. The scotogenic contribution is characterized by the parameter b, and its magnitude is restricted within a narrow range, 0.0048–0.0056 eV. The estimation of DM relic density depends on the scotogenic contribution Yukawa coupling κ associated with $|b|$, as given in Eq. (11). This dependence is shown in Fig. 10 in the DM mass M_f-κ plane. The allowed parameter space gets further constrained to satisfy correct neutrino oscillation data and experimental limits on LFV decays discussed in Secs. IV and VIII, respectively. Although the allowed range of $|b|$ is tightly constrained from neutrino oscillation data, interplay of DM f and other dark sector particles $\eta_{I,R,\pm}$ can satisfy correct DM relic density with contributions from various annihilation and coannihilation contributions mentioned in Figs. 6–8. Hence, updating Fig. 10, in Fig. 16, we have plotted the final parameter space, which includes constraints from DM relic density, neutrino oscillation data, and LFV decays. The points with the color code represent the parameter space consistent with the DM relic density and direct-search constraints. Once we impose the constraints for $|b|$ from the neutrino oscillation data obtained from Fig. 1, we get the magenta-colored points. Finally, we obtain the red star points when we impose the constraint from LFV decays along with the constraints mentioned above from DM

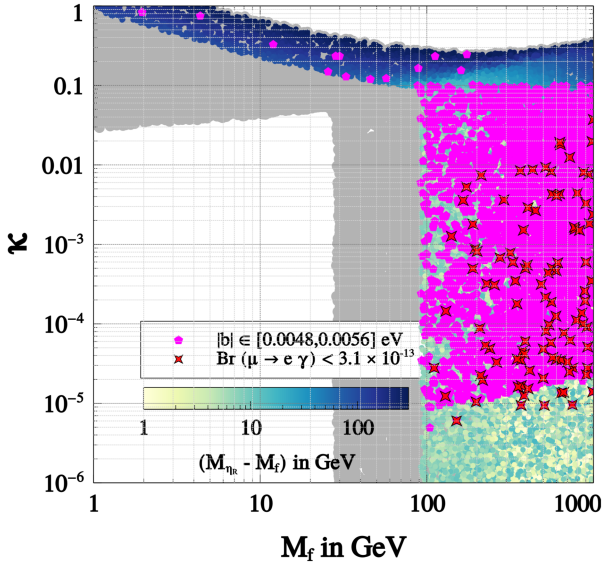

FIG. 16. Final parameter space for the two important parameters of the FSS_1 model—namely, the Yukawa coupling κ and the DM fermion mass M_f—after imposing the constraints from DM relic density, direct search, neutrino oscillation data, and LFV decays.

phenomenology and neutrino oscillation. LFV constraints restrict the maximum allowed Yukawa coupling to be less than $\mathcal{O}(10^{-2})$, and DM masses within (100–1000) GeV are found to be simultaneously consistent with neutrino oscillation data, DM relic density, direct search, and LFV decay constraints.

X. CONCLUSIONS AND OUTLOOK

We propose the flavor-scoto-seesaw (FSS) model, which explains the observed hierarchy between the solar and atmospheric neutrino mass scales, experimentally allows the trimaximal mixing scheme, and naturally accommodates viable dark matter candidates. In this framework, type-I seesaw and one-loop scotogenic mechanisms contribute to the effective light neutrino mass. With only one right-handed neutrino, the type-I seesaw contribution dominantly contributes to generating the atmospheric neutrino mass scale, and the scotogenic contribution (with the involvement of the dark fermion f and scalar η) is mainly responsible for the solar neutrino mass scale. The whole framework is embedded within $A_4 \times Z_4 \times Z_3 \times Z_2$ discrete flavor symmetry predicting the lightest neutrino to be massless and one nonvanishing Majorana phase. The model also contains a few flavon fields to realize the appropriate flavor structure to explain observed neutrino mixing. The inclusion of auxiliary Z_N $(N = 4, 3, 2)$ symmetries is a generic feature of discrete flavor-symmetric models to forbid several unwanted terms, and the charged lepton mass matrix is found to be a diagonal one. These Z_N symmetries are broken down to a dark Z_2 symmetry,

ensuring the stability of dark matter under which only f and η are odd. With a judicious choice of the flavon vacuum alignments, the TM_1 mixing scheme can be realized, and hence we call our flavor-symmetric scoto-seesaw model an FSS_1 model.

The considered flavor symmetry completely dictates the flavor structure of the model and makes it highly predictive. The FSS_1 model provides rich phenomenology for neutrino masses, mixing, LFV decays, and collider studies, and it accommodates potential dark matter candidates with the DM f fermion and η scalar. With both type-I and scotogenic contributions, a rank-2 light neutrino mass matrix is obtained, predicting normal ordering of the light neutrino mass. The presence of flavor symmetry in FSS_1 implies a preference for the higher octant of the atmospheric mixing angle θ_{23}, where the allowed ranges are given by $0.531 \leq \sin^2\theta_{23} \leq 0.544$ and $0.580 \leq \sin^2\theta_{23} \leq 0.595$. The model also tightly constrains the TM_1 prediction for the Dirac CP phase δ_{CP} [within the range $\pm(1.44$–$1.12)$ rad] and the Jarlskog CP invariant. Moreover, correlations among neutrino mixing parameters within the FSS_1 model (see Figs. 3 and 4) give a strict determination of the Majorana CP phase, thus giving an accurate prediction for $m_{\beta\beta}$ (see Table II) within the range 1.61–3.85 meV. Here, the dark fermion f is considered as the DM candidate whose production mechanism is connected with its Yukawa coupling with SM leptons and the inert doublet scalar η. The magnitude of these Yukawa couplings plays a critical role in determining correct neutrino mixing and DM relic density through the thermal freeze-out mechanism. With the flavor structure of the FSS_1 framework, only the scotogenic part contributes to the lepton-flavor-violating decays such as $\mu \to e\gamma$, $\mu \to 3e$. On the other hand, though they are very small, the seesaw part of FSS_1 only contributes to decays such as $\tau \to \mu\gamma$, $\tau \to 3\mu$. Interestingly, owing to the flavor symmetry and vacuum alignment of the flavons, LFV decays such as $\tau \to e\gamma$ and $\tau \to 3e$ are completely disallowed, and any positive signal LFV for these two decays will test the viability of this model. Within the FSS_1 framework, the WIMP DM masses within (100–1000) GeV are simultaneously consistent with the constraints from neutrino oscillation data, DM relic density, direct search, and LFV decays.

The FSS_1 model can also be tested at the colliders via a wide range of phenomenological studies. For example, FSS_1 can contribute to the Higgs boson diphoton decay channel $h \to \gamma\gamma$. Figure 13 shows that M_{η^+} masses up to 1 TeV can have implications at the diphoton Higgs decay channel using the present LHC experimental results. With the increasing data collection at LHC and HL-LHC, the precision of $R_{\gamma\gamma}$ will improve, giving prospects for better determination of allowed regions for specific flavor model parameters. Thus, phenomenology-based $R_{\gamma\gamma}$ constraints can be used for further studies and predictions for producing exotic discrete flavor model signals at present and future colliders. The same statement is valid for further phenomenological studies of the model based on DM and LFV constraints. Thus, in alignment with all pertinent constraints, the model retains its predictiveness across LFV experiments and direct detection of DM, as well as collider experiments.

ACKNOWLEDGMENTS

This work has been supported in part by the Polish National Science Center (NCN) under Grant No. 2020/37/B/ST2/02371, the Freedom of Research (Swoboda Badań), and the Research Excellence Initiative of the University of Silesia in Katowice. B. K. would like to thank José W. F. Valle and Claudia Hagedorn for useful discussions. B. K. also acknowledges hospitality at the Korea Institute of Advanced Study, Seoul, where part of this work has been completed. S. M. acknowledges the financial support from National Research Foundation of Korea Grant No. 2022R1A2C1005050.

APPENDIX: A_4 SYMMETRY

A_4 is a discrete group of even permutations of four objects.[6] Geometrically, it is an invariance group of a tetrahedron. It has 12 elements which can be generated by two basic objects S and T, which obey the following relations:

$$S^2 = T^3 = (ST)^3 = 1. \tag{A1}$$

The A_4 group has three one-dimensional irreducible representations—1, 1′, and 1″—and one three-dimensional irreducible representation—3. Products of the singlets and triplets are given by [27]

$$1 \otimes 1 = 1; \qquad 1' \otimes 1'' = 1, \tag{A2}$$

$$1' \otimes 1' = 1''; \qquad 1'' \otimes 1'' = 1', \tag{A3}$$

$$3 \otimes 3 = 1 \oplus 1' \oplus 1'' \oplus 3_s \oplus 3_a, \tag{A4}$$

where the subscripts "s" and "a" denote symmetric and antisymmetric parts, respectively. Writing two A_4 triplets as $X = (x_1, x_2, x_3)^T$ and $Y = (y_1, y_2, y_3)^T$, respectively, their product can be written as [27]

$$X \otimes Y = (X \otimes Y)_1 \oplus (X \otimes Y)_{1'} \oplus (X \otimes Y)_{1''} \oplus (X \otimes Y)_{3s} \oplus (X \otimes Y)_{3a}, \tag{A5}$$

where

$$(X \otimes Y)_1 \sim x_1 y_1 + x_2 y_3 + x_3 y_2, \tag{A6}$$

[6]For a detailed discussion on A_4, see Refs. [27,28].

$$(X \otimes Y)_{1'} \sim x_3 y_3 + x_1 y_2 + x_2 y_1, \tag{A7}$$

$$(X \otimes Y)_{1''} \sim x_2 y_2 + x_1 y_3 + x_3 y_1, \tag{A8}$$

$$(X \otimes Y)_{3s} \sim \begin{pmatrix} 2x_1 y_1 - x_2 y_3 - x_3 y_2 \\ 2x_3 y_3 - x_1 y_2 - x_2 y_1 \\ 2x_2 y_2 - x_1 y_3 - x_3 y_1 \end{pmatrix}, \tag{A9}$$

$$(X \otimes Y)_{3a} \sim \begin{pmatrix} x_2 y_3 - x_3 y_2 \\ x_1 y_2 - x_2 y_1 \\ x_3 y_1 - x_1 y_3 \end{pmatrix}. \tag{A10}$$

These relations are used in the construction of the mass matrices given in Eqs. (7) and (12).

[1] S. Fukuda *et al.* (Super-Kamiokande Collaboration), Constraints on neutrino oscillations using 1258 days of Super-Kamiokande solar neutrino data, Phys. Rev. Lett. **86**, 5656 (2001).

[2] Y. Ashie *et al.* (Super-Kamiokande Collaboration), A measurement of atmospheric neutrino oscillation parameters by Super-Kamiokande I, Phys. Rev. D **71**, 112005 (2005).

[3] Q. R. Ahmad *et al.* (SNO Collaboration), Direct evidence for neutrino flavor transformation from neutral current interactions in the Sudbury Neutrino Observatory, Phys. Rev. Lett. **89**, 011301 (2002).

[4] Q. R. Ahmad *et al.* (SNO Collaboration), Measurement of day and night neutrino energy spectra at SNO and constraints on neutrino mixing parameters, Phys. Rev. Lett. **89**, 011302 (2002).

[5] S. Abe *et al.* (KamLAND Collaboration), Precision measurement of neutrino oscillation parameters with KamLAND, Phys. Rev. Lett. **100**, 221803 (2008).

[6] K. Abe *et al.* (T2K Collaboration), Indication of electron neutrino appearance from an accelerator-produced off-axis muon neutrino beam, Phys. Rev. Lett. **107**, 041801 (2011).

[7] Y. Abe *et al.* (Double Chooz Collaboration), Indication for the disappearance of reactor electron antineutrinos in the Double Chooz experiment, Phys. Rev. Lett. **108**, 131801 (2012).

[8] K. Abe *et al.* (T2K Collaboration), Observation of electron neutrino appearance in a muon neutrino beam, Phys. Rev. Lett. **112**, 061802 (2014).

[9] M. Aker *et al.* (KATRIN Collaboration), Direct neutrino-mass measurement with sub-electronvolt sensitivity, Nat. Phys. **18**, 160 (2022).

[10] N. Aghanim *et al.* (Planck Collaboration), Planck 2018 results: VI. Cosmological parameters, Astron. Astrophys. **641**, A6 (2020); **652**, C4(E) (2021).

[11] S. Abe *et al.* (KamLAND-Zen Collaboration), Search for the Majorana nature of neutrinos in the inverted mass ordering region with KamLAND-Zen, Phys. Rev. Lett. **130**, 051801 (2023).

[12] P. Minkowski, $\mu \to e\gamma$ at a rate of one out of 10^9 muon decays?, Phys. Lett. **67B**, 421 (1977).

[13] M. Gell-Mann, P. Ramond, and R. Slansky, Complex spinors and unified theories, Conf. Proc. C **790927**, 315 (1979), https://inspirehep.net/literature/9686.

[14] R. N. Mohapatra and G. Senjanovic, Neutrino mass and spontaneous parity violation, Phys. Rev. Lett. **44**, 912 (1980).

[15] R. N. Mohapatra, Mechanism for understanding small neutrino mass in superstring theories, Phys. Rev. Lett. **56**, 561 (1986).

[16] M. Magg and C. Wetterich, Neutrino mass problem and gauge hierarchy, Phys. Lett. **94B**, 61 (1980).

[17] G. Lazarides, Q. Shafi, and C. Wetterich, Proton lifetime and fermion masses in an SO(10) model, Nucl. Phys. **B181**, 287 (1981).

[18] J. Schechter and J. W. F. Valle, Neutrino masses in $SU(2) \times U(1)$ theories, Phys. Rev. D **22**, 2227 (1980).

[19] R. N. Mohapatra and J. W. F. Valle, Neutrino mass and baryon number nonconservation in superstring models, Phys. Rev. D **34**, 1642 (1986).

[20] Y. Cai, J. Herrero-García, M. A. Schmidt, A. Vicente, and R. R. Volkas, From the trees to the forest: A review of radiative neutrino mass models, Front. Phys. **5**, 63 (2017).

[21] F. P. An *et al.* (Daya Bay Collaboration), Observation of electron-antineutrino disappearance at Daya Bay, Phys. Rev. Lett. **108**, 171803 (2012).

[22] J. K. Ahn *et al.* (RENO Collaboration), Observation of reactor electron antineutrino disappearance in the RENO experiment, Phys. Rev. Lett. **108**, 191802 (2012).

[23] I. Esteban, M. Gonzalez-Garcia, M. Maltoni, T. Schwetz, and A. Zhou, The fate of hints: updated global analysis of three-flavor neutrino oscillations, J. High Energy Phys. 09 (2020) 178.

[24] P. F. Harrison, D. H. Perkins, and W. G. Scott, Tri-bimaximal mixing and the neutrino oscillation data, Phys. Lett. B **530**, 167 (2002).

[25] E. Ma and G. Rajasekaran, Softly broken A(4) symmetry for nearly degenerate neutrino masses, Phys. Rev. D **64**, 113012 (2001).

[26] G. Altarelli and F. Feruglio, Tri-bimaximal neutrino mixing, A(4) and the modular symmetry, Nucl. Phys. **B741**, 215 (2006).

[27] H. Ishimori, T. Kobayashi, H. Ohki, Y. Shimizu, H. Okada, and M. Tanimoto, Non-Abelian discrete symmetries in particle physics, Prog. Theor. Phys. Suppl. **183**, 1 (2010).

[28] G. Altarelli and F. Feruglio, Discrete flavor symmetries and models of neutrino mixing, Rev. Mod. Phys. **82**, 2701 (2010).

[29] S. F. King and C. Luhn, Neutrino mass and mixing with discrete symmetry, Rep. Prog. Phys. **76**, 056201 (2013).
[30] S. T. Petcov, Discrete flavour symmetries, neutrino mixing and leptonic *CP* violation, Eur. Phys. J. C **78**, 709 (2018).
[31] G. Chauhan, P. S. B. Dev, B. Dziewit, W. Flieger, J. Gluza, K. Grzanka, B. Karmakar, J. Vergeest, and S. Zieba, Discrete flavor symmetries and lepton masses and mixings, in *2022 Snowmass Summer Study* (2022), 3; arXiv:2203.08105.
[32] G. Chauhan, P. S. B. Dev, I. Dubovyk, B. Dziewit, W. Flieger, K. Grzanka, J. Gluza, B. Karmakar, and S. Zieba, Phenomenology of lepton masses and mixing with discrete flavor symmetries, Prog. Part. Nucl. Phys. **138**, 104126 (2024).
[33] C. H. Albright and W. Rodejohann, Comparing trimaximal mixing and its variants with deviations from tri-bimaximal mixing, Eur. Phys. J. C **62**, 599 (2009).
[34] J. D. Bjorken, P. F. Harrison, and W. G. Scott, Simplified unitarity triangles for the lepton sector, Phys. Rev. D **74**, 073012 (2006).
[35] C. H. Albright, A. Dueck, and W. Rodejohann, Possible alternatives to tri-bimaximal mixing, Eur. Phys. J. C **70**, 1099 (2010).
[36] X.-G. He and A. Zee, Minimal modification to the tri-bimaximal neutrino mixing, Phys. Lett. B **645**, 427 (2007).
[37] C. Luhn, Trimaximal TM_1 neutrino mixing in S_4 with spontaneous *CP* violation, Nucl. Phys. **B875**, 80 (2013).
[38] I. de Medeiros Varzielas and L. Lavoura, Flavour models for TM_1 lepton mixing, J. Phys. G **40**, 085002 (2013).
[39] Y. Shimizu, K. Takagi, and M. Tanimoto, Towards the minimal seesaw model via *CP* violation of neutrinos, J. High Energy Phys. 11 (2017) 201.
[40] B. Thapa and N. K. Francis, Resonant leptogenesis and TM_1 mixing in minimal type-I seesaw model with S_4 symmetry, Eur. Phys. J. C **81**, 1061 (2021).
[41] M. Chakraborty, R. Krishnan, and A. Ghosal, Predictive S_4 flavon model with TM_1 mixing and baryogenesis through leptogenesis, J. High Energy Phys. 09 (2020) 025.
[42] R. de Adelhart Toorop, F. Feruglio, and C. Hagedorn, Discrete flavour symmetries in light of T2K, Phys. Lett. B **703**, 447 (2011).
[43] R. de Adelhart Toorop, F. Feruglio, and C. Hagedorn, Finite modular groups and lepton mixing, Nucl. Phys. **B858**, 437 (2012).
[44] D. Hernandez and A. Y. Smirnov, Discrete symmetries and model-independent patterns of lepton mixing, Phys. Rev. D **87**, 053005 (2013).
[45] G.-J. Ding, TFH mixing patterns, large θ_{13} and $\Delta(96)$ flavor symmetry, Nucl. Phys. **B862**, 1 (2012).
[46] B. Karmakar and A. Sil, Nonzero θ_{13} and leptogenesis in a type-I seesaw model with A_4 symmetry, Phys. Rev. D **91**, 013004 (2015).
[47] B. Karmakar and A. Sil, Spontaneous *CP* violation in lepton-sector: A common origin for θ_{13}, the Dirac *CP* phase, and leptogenesis, Phys. Rev. D **93**, 013006 (2016).
[48] B. Karmakar and A. Sil, An A_4 realization of inverse seesaw: Neutrino masses, θ_{13} and leptonic non-unitarity, Phys. Rev. D **96**, 015007 (2017).
[49] B. Karmakar and A. Sil, Connecting nonzero Θ_{13}, Dirac *CP* phase and leptogenesis through spontaneous *CP* violation, J. Phys. Conf. Ser. **888**, 012177 (2017).
[50] C. Cheung and D. Sanford, Simplified models of mixed dark matter, J. Cosmol. Astropart. Phys. 02 (2014) 011.
[51] G. Hinshaw *et al.* (WMAP Collaboration), Nine-Year Wilkinson Microwave Anisotropy Probe (WMAP) Observations: Cosmological parameter results, Astrophys. J. Suppl. Ser. **208**, 19 (2013).
[52] N. Aghanim *et al.* (Planck Collaboration), Planck 2018 results: VI. Cosmological parameters, Astron. Astrophys. **641**, A6 (2020).
[53] S. F. King, Atmospheric and solar neutrinos with a heavy singlet, Phys. Lett. B **439**, 350 (1998).
[54] S. F. King, Atmospheric and solar neutrinos from single right-handed neutrino dominance and U(1) family symmetry, Nucl. Phys. **B562**, 57 (1999).
[55] S. F. King, Large mixing angle MSW and atmospheric neutrinos from single right-handed neutrino dominance and $U(1)$ family symmetry, Nucl. Phys. **B576**, 85 (2000).
[56] S. F. King, Constructing the large mixing angle MNS matrix in seesaw models with right-handed neutrino dominance, J. High Energy Phys. 09 (2002) 011.
[57] S. Antusch, S. Boudjemaa, and S. F. King, Neutrino mixing angles in sequential dominance to NLO and NNLO, J. High Energy Phys. 09 (2010) 096.
[58] S. Antusch and S. F. King, Sequential dominance, New J. Phys. **6**, 110 (2004).
[59] S. F. King, Predicting neutrino parameters from $SO(3)$ family symmetry and quark-lepton unification, J. High Energy Phys. 08 (2005) 105.
[60] S. Antusch, S. F. King, C. Luhn, and M. Spinrath, Trimaximal mixing with predicted θ_{13} from a new type of constrained sequential dominance, Nucl. Phys. **B856**, 328 (2012).
[61] N. Rojas, R. Srivastava, and J. W. F. Valle, Simplest scoto-seesaw mechanism, Phys. Lett. B **789**, 132 (2019).
[62] J. Leite, S. Sadhukhan, and J. W. F. Valle, Dynamical scoto-seesaw mechanism with gauged $B - L$, Phys. Rev. D **109**, 035023 (2024).
[63] S. Mandal, R. Srivastava, and J. W. F. Valle, The simplest scoto-seesaw model: WIMP dark matter phenomenology and Higgs vacuum stability, Phys. Lett. B **819**, 136458 (2021).
[64] D. M. Barreiros, F. R. Joaquim, R. Srivastava, and J. W. F. Valle, Minimal scoto-seesaw mechanism with spontaneous *CP* violation, J. High Energy Phys. 04 (2021) 249.
[65] J. Ganguly, J. Gluza, and B. Karmakar, Common origin of θ_{13} and dark matter within the flavor symmetric scoto-seesaw framework, J. High Energy Phys. 11 (2022) 074.
[66] Y. Koide, $S(4)$ flavor symmetry embedded into $SU(3)$ and lepton masses and mixing, J. High Energy Phys. 08 (2007) 086.
[67] A. Adulpravitchai, A. Blum, and M. Lindner, Non-Abelian discrete groups from the breaking of continuous flavor symmetries, J. High Energy Phys. 09 (2009) 018.
[68] C. Luhn, Spontaneous breaking of SU(3) to finite family symmetries: A pedestrian's approach, J. High Energy Phys. 03 (2011) 108.

[69] A. Merle and R. Zwicky, Explicit and spontaneous breaking of $SU(3)$ into its finite subgroups, J. High Energy Phys. 02 (2012) 128.

[70] B. L. Rachlin and T. W. Kephart, Spontaneous breaking of gauge groups to discrete symmetries, J. High Energy Phys. 08 (2017) 110.

[71] S. F. King and Y.-L. Zhou, Spontaneous breaking of $SO(3)$ to finite family symmetries with supersymmetry: An A_4 model, J. High Energy Phys. 11 (2018) 173.

[72] G. Altarelli and F. Feruglio, Tri-bimaximal neutrino mixing from discrete symmetry in extra dimensions, Nucl. Phys. **B720**, 64 (2005).

[73] T. J. Burrows and S. F. King, $A(4)$ family symmetry from $SU(5)$ SUSY GUTs in 6D, Nucl. Phys. **B835**, 174 (2010).

[74] S. F. King, Unified models of neutrinos, flavour and CP violation, Prog. Part. Nucl. Phys. **94**, 217 (2017).

[75] F. Feruglio, Are neutrino masses modular forms?, *From My Vast Repertoire…*, (World Scientific, Singapore, 2019), pp. 227–266.

[76] F. J. de Anda, S. F. King, and E. Perdomo, $SU(5)$ grand unified theory with A_4 modular symmetry, Phys. Rev. D **101**, 015028 (2020).

[77] P. P. Novichkov, S. T. Petcov, and M. Tanimoto, Trimaximal neutrino mixing from modular A_4 invariance with residual symmetries, Phys. Lett. B **793**, 247 (2019).

[78] J. C. Criado and F. Feruglio, Modular invariance faces precision neutrino data, SciPost Phys. **5**, 042 (2018).

[79] T. Kobayashi, Y. Shimizu, K. Takagi, M. Tanimoto, T. H. Tatsuishi, and H. Uchida, Finite modular subgroups for fermion mass matrices and baryon/lepton number violation, Phys. Lett. B **794**, 114 (2019).

[80] J. T. Penedo and S. T. Petcov, Lepton masses and mixing from modular S_4 symmetry, Nucl. Phys. **B939**, 292 (2019).

[81] G.-J. Ding, S. F. King, and X.-G. Liu, Neutrino mass and mixing with A_5 modular symmetry, Phys. Rev. D **100**, 115005 (2019).

[82] C. Bonilla, J. Herms, O. Medina, and E. Peinado, Discrete dark matter mechanism as the source of neutrino mass scales, J. High Energy Phys. 06 (2023) 078.

[83] M. Hirsch, S. Morisi, E. Peinado, and J. W. F. Valle, Discrete dark matter, Phys. Rev. D **82**, 116003 (2010).

[84] G. Aad *et al.* (ATLAS Collaboration), Measurement of the properties of Higgs boson production at $\sqrt{s} = 13$ TeV in the $H \to \gamma\gamma$ channel using 139 fb^{-1} of pp collision data with the ATLAS experiment, J. High Energy Phys. 07 (2023) 088.

[85] S. F. King, Neutrino mass and mixing in the seesaw playground, Nucl. Phys. **B908**, 456 (2016).

[86] R. Kumar, P. Mishra, M. K. Behera, R. Mohanta, and R. Srivastava, Predictions from scoto-seesaw with A_4 modular symmetry, Phys. Lett. B **853**, 138635 (2024).

[87] P. Van Dong and D. Van Loi, Scotoseesaw model implied by dark right-handed neutrinos, arXiv:2311.09795.

[88] R. Kumar, N. Nath, and R. Srivastava, Cutting the scotogenic loop: Adding flavor to dark matter, arXiv:2406.00188.

[89] D. Borah, P. Das, B. Karmakar, and S. Mahapatra, Discrete dark matter with light Dirac neutrinos, arXiv:2406.17861.

[90] E. Ma, Quark mass matrices in the A_4 model, Mod. Phys. Lett. A **17**, 627 (2002).

[91] F. Björkeroth and S. F. King, Testing constrained sequential dominance models of neutrinos, J. Phys. G **42**, 125002 (2015).

[92] X.-G. He, Y.-Y. Keum, and R. R. Volkas, A_4 flavor symmetry breaking scheme for understanding quark and neutrino mixing angles, J. High Energy Phys. 04 (2006) 039.

[93] Y. Lin, A predictive A_4 model, Charged lepton hierarchy and tri-bimaximal sum rule, Nucl. Phys. **B813**, 91 (2009).

[94] M. Holthausen and M. A. Schmidt, Natural vacuum alignment from group theory: The minimal case, J. High Energy Phys. 01 (2012) 126.

[95] R. L. Workman *et al.* (Particle Data Group), Review of particle physics, Prog. Theor. Exp. Phys. **2022**, 083C01 (2022).

[96] C. Jarlskog, Commutator of the quark mass matrices in the standard electroweak model and a measure of maximal CP nonconservation, Phys. Rev. Lett. **55**, 1039 (1985).

[97] P. I. Krastev and S. T. Petcov, Resonance amplification and T violation effects in three neutrino oscillations in the earth, Phys. Lett. B **205**, 84 (1988).

[98] P. F. de Salas, D. V. Forero, S. Gariazzo, P. Martínez-Miravé, O. Mena, C. A. Ternes, M. Tórtola, and J. W. F. Valle, 2020 global reassessment of the neutrino oscillation picture, J. High Energy Phys. 02 (2021) 071.

[99] F. Capozzi, E. Di Valentino, E. Lisi, A. Marrone, A. Melchiorri, and A. Palazzo, Unfinished fabric of the three neutrino paradigm, Phys. Rev. D **104**, 083031 (2021).

[100] S. M. Bilenky, J. Hosek, and S. T. Petcov, On oscillations of neutrinos with Dirac and Majorana masses, Phys. Lett. **94B**, 495 (1980).

[101] P. Langacker, S. T. Petcov, G. Steigman, and S. Toshev, On the Mikheev-Smirnov-Wolfenstein (MSW) mechanism of amplification of neutrino oscillations in matter, Nucl. Phys. **B282**, 589 (1987).

[102] J. Gluza and M. Zralek, Parameters' domain in three flavor neutrino oscillations, Phys. Lett. B **517**, 158 (2001).

[103] G. Adhikari *et al.* (nEXO Collaboration), nEXO: Neutrinoless double beta decay search beyond 10^{28} year half-life sensitivity, J. Phys. G **49**, 015104 (2022).

[104] A. Arhrib, R. Benbrik, and N. Gaur, $H \to \gamma\gamma$ in inert Higgs doublet model, Phys. Rev. D **85**, 095021 (2012).

[105] M. Lindner, M. Platscher, C. E. Yaguna, and A. Merle, Fermionic WIMPs and vacuum stability in the scotogenic model, Phys. Rev. D **94**, 115027 (2016).

[106] G. C. Branco, P. M. Ferreira, L. Lavoura, M. N. Rebelo, M. Sher, and J. P. Silva, Theory and phenomenology of two-Higgs-doublet models, Phys. Rep. **516**, 1 (2012).

[107] A. E. C. Hernández, S. F. King, and H. Lee, Fermion mass hierarchies from vectorlike families with an extended 2HDM and a possible explanation for the electron and muon anomalous magnetic moments, Phys. Rev. D **103**, 115024 (2021).

[108] A. E. Cárcamo Hernández, K. Kowalska, H. Lee, and D. Rizzo, Global analysis and LHC study of a vector-like extension of the Standard Model with extra scalars, Phys. Rev. D **109**, 035010 (2024).

[109] T. Aaltonen *et al.* (CDF Collaboration), High-precision measurement of the W boson mass with the CDF II detector, Science **376**, 170 (2022).
[110] K. S. Babu, S. Jana, and Vishnu P. K., Correlating W-boson mass shift with muon $g-2$ in the two Higgs doublet model, Phys. Rev. Lett. **129**, 121803 (2022).
[111] Y.-Z. Fan, T.-P. Tang, Y.-L. S. Tsai, and L. Wu, Inert Higgs dark matter for CDF II W-boson mass and detection prospects, Phys. Rev. Lett. **129**, 091802 (2022).
[112] P. Asadi, C. Cesarotti, K. Fraser, S. Homiller, and A. Parikh, Oblique lessons from the W-mass measurement at CDF II, Phys. Rev. D **108**, 055026 (2023).
[113] A. Strumia, Interpreting electroweak precision data including the W-mass CDF anomaly, J. High Energy Phys. 08 (2022) 248.
[114] G. Arcadi and A. Djouadi, 2HD plus light pseudoscalar model for a combined explanation of the possible excesses in the CDF MW measurement and $(g-2)\mu$ with dark matter, Phys. Rev. D **106**, 095008 (2022).
[115] D. Borah, S. Mahapatra, and N. Sahu, Singlet-doublet fermion origin of dark matter, neutrino mass and W-mass anomaly, Phys. Lett. B **831**, 137196 (2022).
[116] D. Borah, S. Mahapatra, D. Nanda, and N. Sahu, Type II Dirac seesaw with observable $\Delta N_{\rm eff}$ in the light of W-mass anomaly, Phys. Lett. B **833**, 137297 (2022).
[117] D. Borah, S. Mahapatra, P. K. Paul, and N. Sahu, Scotogenic $U(1)_{L_\mu - L_\tau}$ origin of $(g-2)_\mu$, W-mass anomaly and 95 GeV excess, Phys. Rev. D **109**, 055021 (2024).
[118] H.-H. Zhang, W.-B. Yan, and X.-S. Li, The oblique corrections from heavy scalars in irreducible representations, Mod. Phys. Lett. A **23**, 637 (2008).
[119] S. Centelles Chuliá, R. Srivastava, and S. Yadav, CDF-II W boson mass in the Dirac scotogenic model, Mod. Phys. Lett. A **38**, 2350049 (2023).
[120] M. E. Peskin and T. Takeuchi, Estimation of oblique electroweak corrections, Phys. Rev. D **46**, 381 (1992).
[121] ATLAS Collaboration, Improved W boson mass measurement using 7 TeV proton-proton collisions with the ATLAS detector, https://inspirehep.net/literature/2646678.
[122] ATLAS Collaboration, Precise measurements of W and Z transverse momentum spectra with the ATLAS detector at $\sqrt{s} = 5.02$ TeV and 13 TeV, https://inspirehep.net/literature/2775442.
[123] K. Griest and D. Seckel, Three exceptions in the calculation of relic abundances, Phys. Rev. D **43**, 3191 (1991).
[124] G. Belanger, F. Boudjema, A. Pukhov, and A. Semenov, micrOMEGAs3: A program for calculating dark matter observables, Comput. Phys. Commun. **185**, 960 (2014).
[125] E. Aprile *et al.* (XENON Collaboration), Projected WIMP sensitivity of the XENONnT dark matter experiment, J. Cosmol. Astropart. Phys. 11 (2020) 031.
[126] J. Aalbers *et al.* (DARWIN Collaboration), DARWIN: Towards the ultimate dark matter detector, J. Cosmol. Astropart. Phys. 11 (2016) 017.
[127] A. M. Sirunyan *et al.* (CMS Collaboration), Measurements of Higgs boson production cross sections and couplings in the diphoton decay channel at $\sqrt{s} = 13$ TeV, J. High Energy Phys. 07 (2021) 027.
[128] A. Freitas *et al.*, Theoretical uncertainties for electroweak and Higgs-boson precision measurements at FCC-ee, arXiv:1906.05379.
[129] G. Cacciapaglia, A. Deandrea, and J. Llodra-Perez, Higgs → Gamma Gamma beyond the Standard Model, J. High Energy Phys. 06 (2009) 054.
[130] P. Posch, Enhancement of $h \to \gamma\gamma$ in the two Higgs doublet model type I, Phys. Lett. B **696**, 447 (2011).
[131] R. S. Hundi, Implications of Higgs boson to diphoton decay rate in the bilinear R-parity violating supersymmetric model, Phys. Rev. D **87**, 115005 (2013).
[132] R. S. Hundi, Study on the global minimum and H → $\gamma\gamma$ in the Dirac scotogenic model, Phys. Rev. D **108**, 015006 (2023).
[133] M. A. Shifman, A. I. Vainshtein, M. B. Voloshin, and V. I. Zakharov, Low-energy theorems for Higgs boson couplings to photons, Sov. J. Nucl. Phys. **30**, 711 (1979), https://inspirehep.net/literature/141287.
[134] T. Toma and A. Vicente, Lepton flavor violation in the scotogenic model, J. High Energy Phys. 01 (2014) 160.
[135] A. Vicente and C. E. Yaguna, Probing the scotogenic model with lepton flavor violating processes, J. High Energy Phys. 02 (2015) 144.
[136] C. Hagedorn, J. Herrero-García, E. Molinaro, and M. A. Schmidt, Phenomenology of the generalised scotogenic model with fermionic dark matter, J. High Energy Phys. 11 (2018) 103.
[137] K. Afanaciev *et al.* (MEG II Collaboration), A search for $\mu^+ \to e^+\gamma$ with the first dataset of the MEG II experiment, Eur. Phys. J. C **84**, 216 (2024).
[138] U. Bellgardt *et al.* (SINDRUM Collaboration), Search for the decay $\mu^+ \to e^+e^+e^-$, Nucl. Phys. **B299**, 1 (1988).
[139] A. M. Baldini *et al.* (MEG II Collaboration), The design of the MEG II experiment, Eur. Phys. J. C **78**, 380 (2018).
[140] A.-K. Perrevoort (Mu3e Collaboration), The rare and forbidden: Testing physics beyond the Standard Model with Mu3e, SciPost Phys. Proc. **1**, 052 (2019).
[141] B. Aubert *et al.* (*BABAR* Collaboration), Searches for lepton flavor violation in the decays $\tau^\pm \to e^\pm\gamma$ and $\tau^\pm \to \mu^\pm\gamma$, Phys. Rev. Lett. **104**, 021802 (2010).
[142] K. Hayasaka *et al.*, Search for lepton flavor violating τ decays into three leptons with 719 million produced $\tau^+\tau^-$ pairs, Phys. Lett. B **687**, 139 (2010).